Marine and Petroleum Geology 132 (2021) 105169

Contents lists available at ScienceDirect

Marine and Petroleum Geology

journal homepage: www.elsevier.com/locate/marpetgeo

Fracture distribution in a folded fluvial succession: The Puig-reig anticline (south-eastern Pyrenees)

Xiaolong Sun [a], Enrique Gomez-Rivas [a,*], Juan Alcalde [b], Juan Diego Martín-Martín [a], Cunfei Ma [c], Daniel Muñoz-López [a], David Cruset [b], Irene Cantarero [a], Albert Griera [d], Anna Travé [a]

[a] Departament de Mineralogia, Petrologia I Geologia Aplicada, Facultat de Ciències de La Terra, Universitat de Barcelona (UB), C/ Martí I Franquès S/n, Barcelona, 08028, Spain
[b] Geosciences Barcelona (GEO3BCN-CSIC), Lluís Solé I Sabarís S/n, Barcelona, 08028, Spain
[c] School of Geosciences, China University of Petroleum (East China), Qingdao, 266580, China
[d] Departament de Geologia, Universitat Autònoma de Barcelona, Cerdanyola Del Vallès, 08193, Spain

ARTICLE INFO

Keywords:
Fractures
Fluvial fan
Structural position
Fold
Pyrenees

ABSTRACT

Sedimentary rocks of foreland fold-and-thrust belts typically undergo intensive fracturing as folds grow. The resulting fracture networks can present significant variations depending on the distribution of sedimentary facies and the complex structural characteristics of fold-and-thrust belts. The Puig-reig anticline, located in the south-eastern Pyrenees, mainly exposes proximal fluvial deposits in the north limb and medial fluvial deposits in the rest of the anticline. Thus, this anticline constitutes an excellent case study to investigate the main controls on the distribution of fracture networks in folded fluvial deposits, in terms of structural position and lithofacies variations. Outcrops were selected to be representative of different structural positions, from the fold hinge to its limbs, and of a variety of the main lithofacies, from proximal to medial fluvial deposits. Fracture data were acquired using the linear scanline method. The results indicate that the anticline rocks have been affected by four sets of fractures. The north limb is dominated by thick conglomerate bodies with interlayered sandstones deposited from unconfined flash floods and wide-shallow channel streams in the proximal fluvial fan, and presents large fracture spacing and low fracture intensity but relatively large fracture length and aperture. The crest and the crest-limb transition zones are mainly characterised by interlayered conglomerates, sandstones, siltstones and clays, deposited from braided channel streams and overbanks in the medial fluvial fan, and present fractures with relatively high fracture intensity and variable fracture length and aperture. The south limb, composed of channel filling sandstone layers and stable overbank fine deposits in the medial fluvial fan, is characterised by low fracture intensity and small fracture length and aperture. Based on multiple linear regression analysis, fracture intensity is mainly controlled by the structural position, bedding thickness and lithological associations, with relatively more intense fracturing in thin sandstone layers with multiple interlayers of fine deposits in the anticline crest. The fracture length mainly depends on bedding thickness and is affected lithological associations. The fracture apertures are mainly controlled by lithofacies, with relatively higher apertures affecting conglomerate bodies. The results of this study are relevant for characterising similar systems in the subsurface, where data is scarce.

1. Introduction

Fracture networks in rocks of gently deformed foreland basins and intensively deformed fold-and-thrust belts promote the formation of vertical and/or lateral fluid migration pathways within different hydrostratigraphic units (Travé et al., 2007; Fischer et al., 2009; Evans and Fischer, 2012; Evans et al., 2012; Ogata et al., 2014; Muñoz-López et al., 2020a). Many studies have analysed factors controlling the distribution of fracture networks, particularly how the structural position and the characteristics of sedimentary rocks impact the resulting fracture networks (Underwood et al., 2003; Florez-Niño et al., 2005; Lorenz et al., 2006; Wennberg et al., 2006; Ortega et al., 2010; Ogata et al.,

* Corresponding author.
E-mail address: e.gomez-rivas@ub.edu (E. Gomez-Rivas).

https://doi.org/10.1016/j.marpetgeo.2021.105169
Received 12 May 2021; Accepted 31 May 2021
Available online 4 June 2021

2017). Here we use the term 'fracture' in a wide sense to refer to discrete mechanical discontinuities in the rock mass formed under the action of stress, including low- or zero-offset fractures, joints, microfractures and veins (*i.e.*, sealed fractures) (Peacock et al., 2016), and leave out high-offset faults within large fault zones.

Fracture network attributes, including fracture intensity, orientation, length, aperture and connectivity have been described to be closely related to the structural position of a rock volume within a fold (Peacock, 2001; Bellahsen et al., 2006; Ghosh and Mitra, 2009; Watkins et al., 2015a). In asymmetric folds, fracture networks in fold hinges or forelimbs tend to have high intensity, with fractures presenting wider apertures and better connectivity than those located in fold backlimbs, due to the greater curvature and finite strain (Nelson and Serra, 1995; Watkins et al., 2015a). Besides, fracture intensity tends to increase in the proximity of large faults (Cooper et al., 2006). Other studies show that the intensity of certain fracture sets can vary with the structural position and finite strain, while in other sets it may show less variation across fold sections. Some examples are the Oil Mountain anticline in Wyoming (Hennings et al., 2000) and the Teton anticline in Montana (Ghosh and Mitra, 2009). Additionally, fractures formed prior to folding can contribute to the mechanical anisotropy of stratified units and thus significantly impact the resulting fracture networks formed during fold growth. For example, the Emigrant Gap anticline in Wyoming features constant fracture characteristics owing to the influence of pre-folding fractures (Bergbauer and Pollard, 2004). All these previous studies point out that the position with respect to a structural feature can be a key factor controlling fracture attributes, but there is great variability in their relationship.

Apart from the structural position, the characteristics of the hosting sedimentary rocks have also been reported to be key controls on the distribution of fracture networks. The depositional and diagenetic characteristics of a rock unit, including the lithofacies architecture, lithological assemblages, bedding thickness, depositional components, textures, grain size and presence of cements and other diagenetic products determine the rock mechanical properties, including stiffness, cohesion and angle of internal friction (Shackleton et al., 2005; Olson et al., 2007; Ferrill and Morris, 2008; Laubach et al., 2009). Some studies reported a clear negative correlation between fracture intensity and bedding thickness (Huang and Angelier, 1989; Florez-Niño et al., 2005; Wennberg et al., 2007), while others did not reveal systematic relationships (Guiton et al., 2003; Wennberg et al., 2006; Ortega et al., 2010; Awdal et al., 2013). Competent rocks, such as clay-poor carbonates, are typically associated with much higher fracture intensity than clay-rich rocks (Ferrill and Morris, 2008). Grain size has a significant effect on fracture propagation, in a way that increasing grain size has been found to reduce crack coalescence and crack damage thresholds (Eberhardt et al., 1999). The rock mechanical properties can also greatly evolve with progressive diagenetic events, thus affecting the evolution of fracture networks (Di Naccio et al., 2005; Laubach et al., 2009; Barbier et al., 2012).

Foreland basins and their adjacent fold-and-thrust belts contain significant hydrocarbon resources (Mann et al., 2003), and also show high potential for CO_2 storage (Sun et al., 2020). As important fluid migration pathways and potential reservoir space, fracture networks have been widely studied in thrust belts composed of carbonate deposits due to their abundant hydrocarbon resources, *e.g.*, in the Zagros fold-and-thrust belt (Stephenson et al., 2007), the Bighorn Basin (Bellahsen et al., 2006), the Apennines (Van Dijk et al., 2000) and the Oman Mountains (Gomez-Rivas et al., 2014), among other areas. However, studies of fracturing of thrust belts composed of sandstone deposits are significantly less well documented (Watkins et al., 2015a). An example of understudied systems is alluvial-fluvial fans, which are the main deposits in non-marine foreland basins at their active margins (Horton and Decelles, 2001).

The southern Pyrenees presents multiple fold and thrust related alluvial-fluvial fans, which are buried as subsurface reservoirs or exposed as outcrops (*e.g.*, Arenas et al., 2001; Jones, 2004; Sáez et al., 2007; Yuste et al., 2004). Such alluvial-fluvial strata in the subsurface show high potential to become effective reservoirs. For example, the eastern part of the Puig-reig anticline in the south-eastern Pyrenees was assessed as a potential site for gas storage (Instituto Geológico y Minero de España, 1995). Besides, the well-exposed outcrops can provide excellent reservoir analogues to investigate fracture distributions in folded alluvial-fluvial successions at basin margins. However, most studies of the southern Pyrenees focused on unravelling the different tectonic events and/or analysing the fingerprints of fluids to decipher the evolution of fluid flow (Travé et al., 2000; Beaudoin et al., 2015; Taillefer et al., 2017; Cruset et al., 2018, 2020, 2020; Lacroix et al., 2018; Nardini et al., 2019; Muñoz-López et al., 2020b), while only a few studies focused on the formation or distribution of fractures (*e.g.,* Tavani et al., 2011, 2020; Gutmanis et al., 2018). Here we present a systematic analysis of the fracture network of a folded fluvial succession exposed in the Puig-reig anticline. Fracture attributes from different structural positions and sedimentary facies were collected and analysed, with the overarching aim of determining what are the main depositional and structural controls on fracture distributions.

2. Geological setting

The Pyrenees is a doubly verging orogenic belt that formed during the continental collision between the Iberian and European plates from the Late Cretaceous to the Miocene (Muñoz, 1992; Vergés et al., 2002). This orogenic belt is characterised by an antiformal stack of basement-involved thrusts (the Axial Zone) surrounded by two fold-and-thrust belts that were transported to the north and south over the Aquitanian (France) and Ebro (Spain) foreland basins, respectively (Choukroune, 1989; Roure et al., 1989; Muñoz, 1992). The eastern part of the Ebro Basin displays an irregular shape bounded by the Pyrenees to the north and the Catalan Coastal Range to the southeast (Fig. 1A and B) (Vergés, 1993; Vergés et al., 1998). The Vallfogona thrust represents the major frontal thrust between the SE Pyrenean thrust sheets and the Ebro Basin. The Busa syncline and the Puig-reig anticline developed along the footwall of the Vallfogona thrust during the Late Eocene and Oligocene (Vergés, 1993).

Based on the available seismic profiles across the Puig-reig anticline (Fig. 1C), the anticline was interpreted to have been formed as a consequence of a duplex stack in depth (Vergés, 1993). In the lower part, the Banyoles and Igualada Formations (Middle-to-Upper Eocene) consist of marine marls. They were duplicated by thrusting and detached above the Beuda evaporitic formation (Middle Eocene) (Vergés et al., 1992; Serra-Kiel et al., 2003a, 2003b). In the upper part, the Berga Group and the Solsona Formation (Upper Eocene to Oligocene) were deposited during the endorheic stage of the Ebro Basin (Puigdefàbregas et al., 1986, 1992), after a rapid transition from marine to continental environments of deposition at around 36 Ma during the Priabonian (Costa et al., 2010). During the Oligocene, the Vallfogona footwall was folded forming the km-scale south-verging gentle anticline of Puig-reig. The fold-trend is ESE/WNW, slightly oblique to the main Pyrenean structures (Vergés, 1993).

To the north, at the footwall of the Vallfogona thrust, the Berga Group consists of more than 2000 m-thick alluvial and proximal fluvial conglomerates interbedded with minor sandstones and claystones, which display growth strata geometries (Ford et al., 1997; Suppe et al., 1997). To the south, the Berga deposits became progressively finer-grained and thinner-bedded fluvial conglomerates, sandstones and claystones of the Solsona Formation (Williams et al., 1998; Barrier et al., 2010). Finally, the Solsona deposits evolved downstream to terminal deposits of a distal fluvial system, which graded into evaporites and calcareous lacustrine sediments towards the centre of the Ebro Basin (Del Santo et al., 2000; Sáez et al., 2007; Barrier et al., 2010).

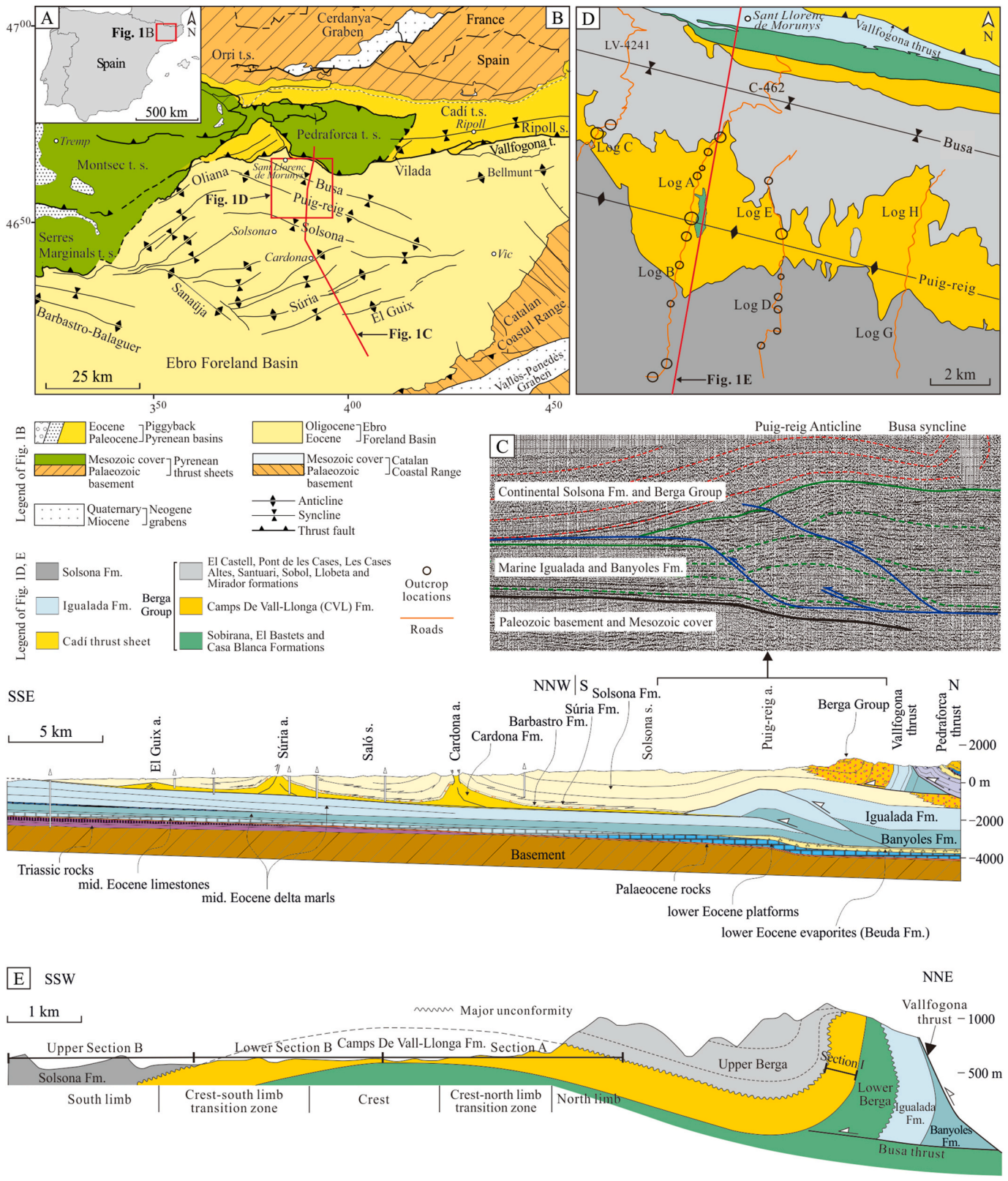

Fig. 1. (A–B) Geographical location and main structural units of the SE Pyrenean fold-and-thrust belt (Vergés, 1993). (C) Geological cross section of the frontal part of the SE Pyrenean fold-and-thrust belt and the Ebro Basin (Vergés, 1993). The seismic profile (Line S-2) is from the Spanish Geophysical Information System (SIGEOF) (Instituto Geológico y Minero de España, 1977). (D–E) Distribution of the Berga Group and the Solsona Formation and location of outcrops. The strata distribution in D is based on the regional geological map of Catalonia (Institut Cartogràfic i Geològic de Catalunya, 2006). The formation subdivision of the Berga Group follows the scheme of Williams et al. (1998). Fig. 1E is modified from Williams et al. (1998) and Barrier et al. (2010).

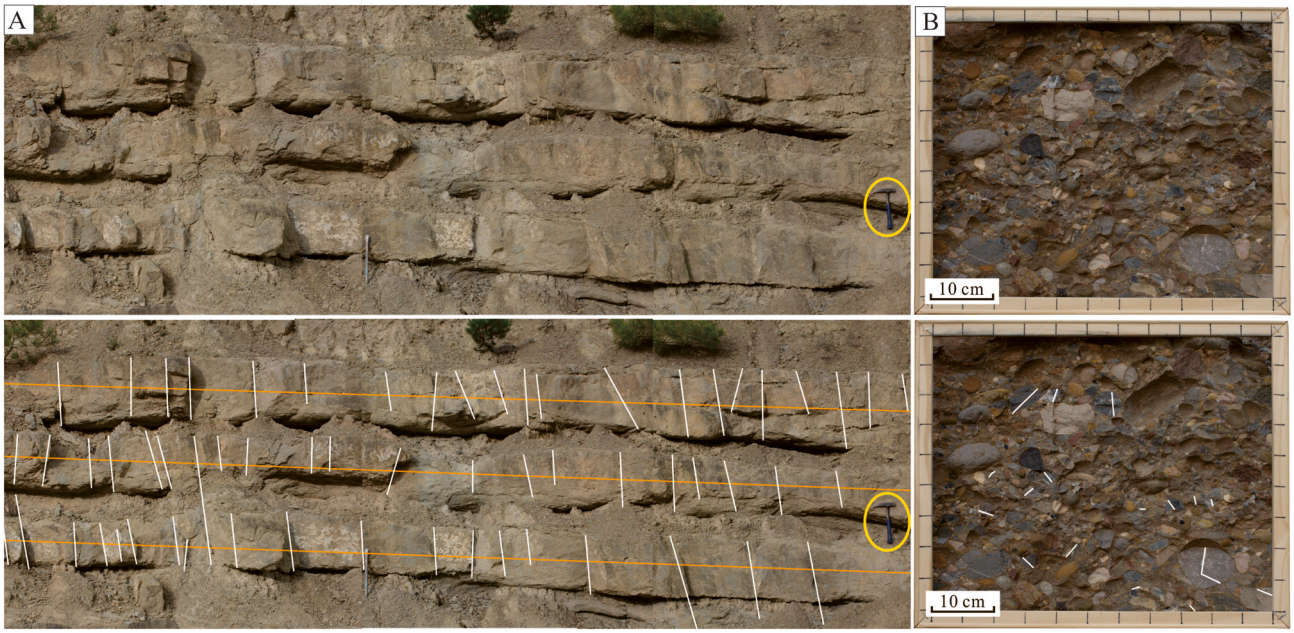

Fig. 2. Examples of outcrop photographs highlighting the different fracture collecting methods: (A) linear scanline method for large and intermediate fractures; (B) window sampling method for small fractures in conglomerates. Orange and white lines represent linear scanlines and identified fractures, respectively. (For interpretation of the references to colour in this figure legend, the reader is referred to the Web version of this article.)

3. Data and methods

The Puig-reig anticline exposes excellent outcrops along four roads perpendicular to the axial direction of the structure, roughly in a north-south direction, between the villages of Sant Llorenç de Morunys in the north and Solsona in the south (Fig. 1B and D). Seven high-resolution stratigraphic logs with a total length of over 3000 m were built based on the data collected from outcrops along these roads (Fig. 1D). Our study mainly focuses on the Camps de Vall-Llonga (a sub-formation of the Berga formation) and Solsona formations (Upper Eocene to Lower Oligocene; Carrigan et al., 2016), which cover most areas of the anticline. The ca. 9 km-long geological cross-section of the Puig-reig anticline (sections A and B, Fig. 1E) lies roughly parallel to the thrust direction of the south-eastern Pyrenees and displays the transition from proximal to medial fluvial deposits.

Three main sampling methods for collecting fracture data are widely used and discussed in the literature, namely the linear scanline, window sampling and circular scanline methods (*e.g.*, Zeeb et al., 2013a, 2013b; Watkins et al., 2015b; Healy et al., 2017 and references thereof). The linear scanline method was adopted in this study because of the nearly vertical outcrops present in the Puig-reig anticline (Fig. 2A), which prevented the use of other fracture sampling methods. The linear scanline method is a fast technique for recording a wide range of fracture attributes (listed in Table 1), including fracture orientation, length, spacing, intensity, aperture and fracture filling. The scanline locations were chosen to be representative of different structural positions as well as of different sedimentary facies and stratigraphic arrangements (*e.g.*, variable bed thickness, lithological associations, etc.). We acquired data from 53 scanlines that add up to around 1600 m in total scanline length (Table 2), along the three western-most roads (Fig. 1C). The fracture data was acquired in groups of at least two people, with the aim of reducing subjective acquisition biases (Andrews et al., 2019). Around 1800 fractures with lengths greater than 20 cm intersecting the scanlines were measured. We did not include large faults with high offsets and obvious fault zones. Small-scale fractures (with length smaller than 20 cm) were difficult to collect using the linear scanline method, especially in conglomerate layers containing abundant fractures confined to only one or a few clasts. To overcome this limitation, the window sampling method was used in zones with abundant small-scale fractures. Conglomerate layers from different structural positions were photographed using a rectangle frame with size dimensions of 45 × 55 cm (Fig. 2B). Cracked clasts located inside the frame were identified and such fracture data manually collected. The intensity of fractured clasts in conglomerates was defined as the ratio of the number of fractured clasts with respect to the number of identifiable clasts. Although we could not quantitatively distinguish fold-related fractured clasts from clasts in other times, such as those with fractures inherited from the source rocks or formed during clast transport, we assume a similar proportion of non-fold-related fractured clasts in different areas. Thus, we only used the intensity of fractured clasts in conglomerates as an indicator to show the relative fracture intensity in different structural positions.

To study fracture-filling cements, vein samples were collected from different structural positions. 60 polished thin sections of calcite veins were

Table 1
Definition of the fracture attributes collected and used in this study based on Zeeb et al. (2013a).

Attribute	Definition
Orientation	Orientation of a fracture on a sampling plane, including strike, dip direction and dip
Length	Length of the fracture trace on a sampling plane (m)
Spacing	Distance between two adjacent fractures (m)
Intensity(scanline)	Number of fractures per unit length (m^{-1})
Intensity(window)	Ratio of the number of fractured clasts to the number of identifiable clasts in a conglomerate sampling window
Aperture	Distance between the two walls of a fracture (mm)
Filling	Mineral precipitate filling fracture porosity to form a vein. This determines whether a fracture acts as a conduit or barrier for fluid flow

Table 2
Location, structural position and sedimentary characteristics of the selected linear scanlines.

Structural position	Sedimentary facies	Typical lithofacies	Thickness (m)	Number of scanline	Length of scanline (m)	Number of fracture	Location
North limb	Proximal fluvial fan	Tabular conglomerate bodies	>3	6	281	98	Log C
		Conglomerate bodies with interlayers	1–4	8	302	271	Logs A, C, E
		Tabular sandstone interlayers	1–2.7	3	58	62	Log E
Crest-North limb transition zone	Medial fluvial fan	Channelised conglomerate bodies	1–4	2	42	83	Log A
		Tabular massive medium to coarse sandstones	0.5–1	2	26	42	Log A
		Tabular bedding fine to very fine sandstones	0.7–1.7	2	28	36	Log A
Crest		Channelised conglomerate bodies	1–3	5	162	257	Logs A, B, E
		Tabular massive medium to coarse sandstones	0.7–1.6	6	147	315	Logs A, B, E
		Tabular bedding fine to very fine sandstones	0.35–2	4	101	195	Logs A, E
Crest-South limb transition zone		Channelised conglomerate bodies	1.3–3	4	127	127	Logs B, D
		Tabular massive medium to coarse sandstones	0.5–0.8	1	7	10	Log D
		Tabular bedding fine to very fine sandstones	1.2–1.8	2	41	74	Log B
South limb		Channelised (pebbly) sandstone bodies	0.5–2	4	186	120	Logs B, D
		Tabular bedding fine to very fine sandstones	0.6–2	4	125	145	Logs B, D

made for petrographic analysis, which was carried out using a Zeiss Axiophot optical microscope and a Technosyn Cold Cathodoluminescence microscope, model 8200 Mk5-1 operating 16–17 kV and 270–290 μA gun current. Furthermore, the geochemical results reported in Cruset et al. (2016) were incorporated into this study. The petrographic analysis in this study together with the geochemical analysis of Cruset et al. (2016) have allowed recognizing different generations of veins, which were combined with the field observations to explain the characteristics of veins in different lithofacies.

4. Results

4.1. Anticline structure

The Puig-reig anticline trends ESE/WNW and has a wavelength of more than 10 km. The ca. 9 km-long geological cross-section (sections A and B in Fig. 1E) exposes continuous outcrops in different structural positions. In this study, the anticline was divided into five structural positions from north to south, namely north limb, crest-north limb transition zone (NTZ), crest, crest-south limb transition zone (STZ) and south limb (Fig. 1E). We did not use the terms proximal and distal to refer to structural positions, as other previous studies did (*e.g.,* Ge et al., 1997; Martínez-Martínez et al., 2002), to avoid the potential confusions with common terms to divide environments of deposition in sedimentary systems (i.e., proximal, medial and distal).

Bedding dip mainly ranges from 5° to 15° in the anticline crest, towards the north in sections A, C, E and H and towards the south in sections B, D and G. The orientation of the fold hinge was estimated based on the distribution of bedding attitudes in the anticline crest, with a resulting strike of 105°. In the anticline crest a system of fractures was observed, including abundant joints and some strike-slip and normal faults with displacements smaller than 20 m and a few small low-angle reverse faults with displacements lower than 2 m, and previously observed also in other studies (Cruset et al., 2016). In the NTZ and north limb of the anticline, the strata mainly dip between 10° to 25° and between 10° to 20°, respectively, towards the north. In the STZ and south limb of the anticline, the strata mainly dip between 15° to 35° and between 10° to 15°, respectively, towards the south. These structural positions are characterised by joints and occasional strike-slip faults.

4.2. Sedimentology

The Camps de Vall-Llonga and Solsona Formations in the Puig-reig anticline were deposited as part of proximal to medial deposits of a fluvial fan system. The north limb is dominated by proximal fluvial deposits characterised by unconfined flash floods and wide-shallow channel streams. Clast- or reddish matrix-supported pebble to cobble conglomerates are the prevailing deposits, especially in the northwest of the anticline. The conglomerate bodies tend to present a massive structure, thick sheet geometries, unscoured or scoured basal surfaces, and broad distributions ranging from a few hundred meters up to 3 km. Fine to coarse sandstone interlayers display stable tabular geometries or pinch out laterally as sandstone lenses. The NTZ, crest and STZ of the anticline are dominated by medial fluvial deposits characterised by braided channel streams and overbanks. These deposits are composed of interlayers of conglomerates, sandstones, siltstones and clays. Channel lag deposits are dominated by clast-supported pebble to small cobble conglomerates with grey sand matrix. The conglomerates commonly present a massive structure, scoured basal surfaces, and channelised geometries. The interlayers of massive and laminated sandstones and overbank fine deposits tend to have tabular geometries. The south limb is also dominated by medial fluvial sediments. However, the conglomerate channel lags are replaced by (pebbly) sandstone channel lags, and the south limb is composed of more fine deposits from overbanks than the NTZ, crest and STZ. The distal fluvial fan is located southward of our study area, and is composed of terminal lobes representing low lake-level stages and fluvial-dominated deltas and interdistributary bays representing high lake level stages (Sáez et al., 2007).

4.3. Fracture attributes

4.3.1. Fracture orientation

Four fracture sets (F1, F2, F3 and F4) were identified in the Puig-reig anticline (from a total 1778 fractures measured) based on fracture orientation and their relationships with the fold hinge (Fig. 3 A). The F1 and F2 sets are oriented NNW-SSE and ENE-WSW, respectively. They are the predominant fracture sets observed at the target structure, accounting for 44% and 28% of the total fractures analysed, respectively. The F3 set is characterised by a WNW-ESE orientation and strikes roughly parallel to the anticline hinge. This set is less frequent and accounts for 17% of the total fractures. The F4 set with a NNE-SSW orientation is very limited along the selected scanlines, because they are sub-parallel to the directions of most scanlines. The lack of outcrops located parallel to bedding planes prevents the identification of systematic termination relations between the different fracture sets, thus making it very difficult to establish their relative ages. The predominance of fracture sets varies depending on the structural position of the outcrop within the anticline (Fig. 3A and B). The F1 set predominates in the north limb and NTZ, which also host a small amount of the other sets. Compared to other structural positions, the fold crest is dominated

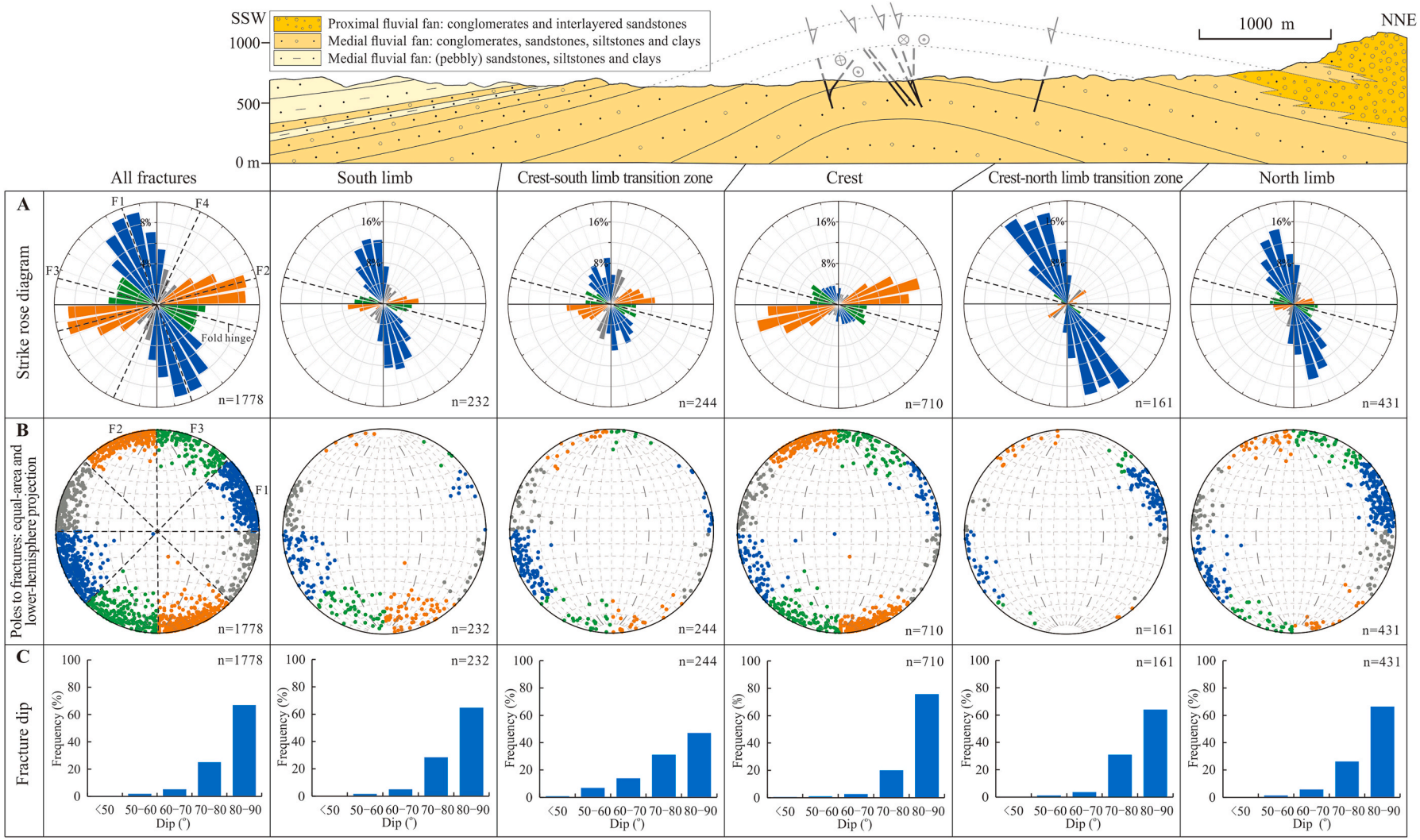

Fig. 3. (A) Rose diagrams displaying fracture strike, (B) stereograms showing fracture 3D orientation and (C) histograms showing fracture dip distribution for different structural positions. The cross section of the Puig-reig anticline is modified from Cruset et al. (2016).

by the F2 set although F1 and F3 sets are also present. From the fold crest to the south limb, the proportion of the F1 set increases significantly while the proportion of the F2 set decreases accordingly. All fractures present high dips, mostly ranging from 70° to 90° (92% of the fractures) (Fig. 3C) and tend to be sub-perpendicular to the bedding surfaces.

4.3.2. Fracture spacing, intensity and length

We consider the apparent fracture spacing as the distance between two adjacent fractures independently of their orientations. The apparent fracture spacing shows variation across the different structural positions (Fig. 4A). The crest and NTZ feature smaller fracture spacing than other zones of the anticline (0.55 m on average *vs.* 1.19 m on average for the other zones). The STZ presents similar spacing distribution but slightly larger overall spacing (0.88 m on average) than the crest and NTZ. In contrast, the north and south limbs conspicuously present larger fracture spacing than the other structural positions (1.55 m and 1.23 m on average, respectively). Fracture spacing also varies significantly depending on the sedimentary lithofacies. The proximal fluvial fan presents larger fracture spacing distributions compared to the medial fluvial fan, mainly ranging between 0.4 m and 3 m, with the largest fracture spacing developing in tabular conglomerate bodies. The medial fluvial fan in the NTZ, crest and STZ presents smaller fracture spacing, especially in tabular massive or bedding sandstone layers, generally smaller than 1 m. The medial fluvial fan in the south limb has larger fracture spacing, mainly between 0.4 m and 2 m, with larger values within the channelised (pebbly) sandstone bodies compared to tabular bedding sandstone layers (Fig. 5A). The cumulative distribution of fracture spacing fits a log-normal distribution (Fig. 6A). Although fracture spacing has a wide range from nearly 0 up to 10 m, it presents a narrow predominant range with 65% of the fracture spacings ranging from 0.2 to 1.2 m.

The apparent fracture intensity is the reciprocal of the apparent fracture spacing, showing the same distribution pattern. The crest presents the highest average fracture intensity (2 m^{-1}) followed by the NTZ (1.66 m^{-1}) and STZ (1.32 m^{-1}), while the south and north limbs present lower fracture intensity (0.94 m^{-1} and 0.70 m^{-1}, respectively) (Fig. 7A). The intensity of fractured clasts of conglomerate layers presents a similar distribution pattern as that of the apparent fracture intensity, with relatively higher values in the crest and NTZ (13.9% and 13.5%, respectively). The apparent fracture intensity also varies significantly in different sedimentary facies and lithofacies (Fig. 7B). The medial fluvial fan in the NTZ, crest and STZ presents the highest average fracture intensity, especially in massive or well-bedded sandstone layers (1.94 m^{-1}), while the proximal fluvial fan in the north limb and the medial fluvial fan in the south limb have lower intensity, especially for tabular conglomerate bodies and channelised (pebbly) sandstone bodies (0.33 m^{-1} and 0.63 m^{-1}, respectively). There can be an underestimation of the intensity of fracture sets intersecting scanlines at oblique angles because the apparent fracture spacing in these cases is higher than the true spacing (Zeeb et al., 2013a; Watkins et al., 2015b). This can be corrected with respect to the angle formed by the fracture and the scanline (Terzaghi, 1965):

$$I = \frac{1}{S_t} = \frac{1}{S_a \times \cos\theta} \quad (1)$$

where I is the true intensity of different fracture sets, S_t is the true fracture spacing, S_a is the apparent fracture spacing, and θ is the acute angle of fracture and scanline. The F4 set is sub-parallel to the directions of most scanlines, resulting in limited fractures intersecting scanlines and very small acute angles between fractures and scanlines. The corrected intensity is too sensitive to the number of fractures and the acute angles, leading to high uncertainty to the results. Thus, we only corrected the fracture intensity of the F1, F2 and F3 sets using this method. The F1 set presents high intensity in all structural positions, while the F2 and F3 sets mainly present high intensity in the crest and STZ of the anticline (Fig. 8A). Similar to the distribution of the apparent fracture intensity, the sum of the true fracture intensity of the three sets results in the highest intensity in the crest (2.38 m^{-1}) followed by the NTZ (1.68 m^{-1}) and STZ (1.56 m^{-1}), while the south limb and north limb correspond to the lowest intensity (1.02 m^{-1} and 0.85 m^{-1}, respectively) (Fig. 8A). Besides, the sum of the true fracture intensity varies significantly in different sedimentary facies and lithofacies (Fig. 8B). The massive or bedded sandstone layers of the medial fluvial fan in the NTZ, crest and STZ have the highest true fracture intensity, with 2.49 m^{-1} and 1.92 m^{-1} on average, respectively. The tabular conglomerate bodies in the north limb and the channelised (pebbly) sandstone bodies in the south limb show the lowest values, with 0.31 m^{-1} and 0.69 m^{-1} on average, respectively.

Fracture length varies from several decimetres to up to 10 m, but mainly ranges between 0.5 m and 2.5 m (for 74% of the fractures) (Fig. 4C). Although there is no clear relationship between the fracture length and the structural position in which fractures are located, the north limb presents larger fracture length (1.52 m on average) compared to the other structural positions within the anticline, while the south limb features the smallest fracture length (1.27 m on average) (Fig. 4C). The proximal fluvial fan in the north limb and the medial fluvial fan in the south limb present the largest and smallest fracture length, respectively. The fracture length of the medial fluvial fan in the NTZ, crest and STZ has values in between those of the other two facies (1.39 m on average). Furthermore, channelised conglomerate bodies tend to present longer fractures than sandstone layers (1.52 m and 1.30 m on average, respectively) (Fig. 5B). Fracture length distributions should normally be corrected for size bias, because the probability of small fractures to cut the scanline is significantly lower than that of large fractures, causing an underestimation of short fractures on the statistical distribution of the whole network (Zeeb et al., 2013a). The probability of collecting fractures greater than or equal to a certain length can be corrected according to the longest fracture length (Zeeb et al., 2013a). The corrected dataset does not fit to an exponential or a power-law distribution, and only a log-normal one presents a reasonable good fit (Fig. 6B).

4.3.3. Fracture aperture and filling

Fracture apertures resulting from stress related to the anticline growth could have potentially been affected by the subsequent stress release during the uplift and exhumation of the anticline. To avoid this uncertainty, in this study we only focus on fractures (now veins) filled with calcite cement precipitated during the anticline growth, where vein widths can represent fracture apertures not affected by the subsequent rock uplift and exhumation. Fracture apertures mainly range from 1 to 5 mm and present significant variation across the different structural positions (Fig. 4C). The north limb presents the largest fracture aperture, which mainly ranges between 1 mm and 5 mm but sometimes reaches up to several centimetres. The crest, NTZ and STZ present similar fracture aperture distributions that mainly range from 1 to 3 mm. The south limb has the smallest fracture aperture with all aperture values below 2 mm. Moreover, fracture aperture also varies significantly across the different sedimentary facies and lithofacies. Fractures in the proximal fluvial fan, especially within the conglomerate bodies with interlayered sandstones, present distinctively large apertures, mainly ranging from a few millimetres to a few centimetres. In the crest, NTZ and STZ, channelised conglomerate bodies present wider fractures (1.99 mm on average) than sandstone layers (1.41 mm on average). In the south limb, fracture apertures of the medial fluvial fan rocks are lower than 2 mm (Fig. 5C). Fracture apertures present a good fit to a power-law in a cumulative distribution plot (Fig. 6C). This fit becomes very clear if the highest fracture apertures (≥3 cm) are not included, which are locally developed in the upper part of log C and filled with large calcite veins, i.e., Cc3 defined below.

Four generations of veins have been identified based on their petrographic characteristics. The first generation of calcite cement (Cc1)

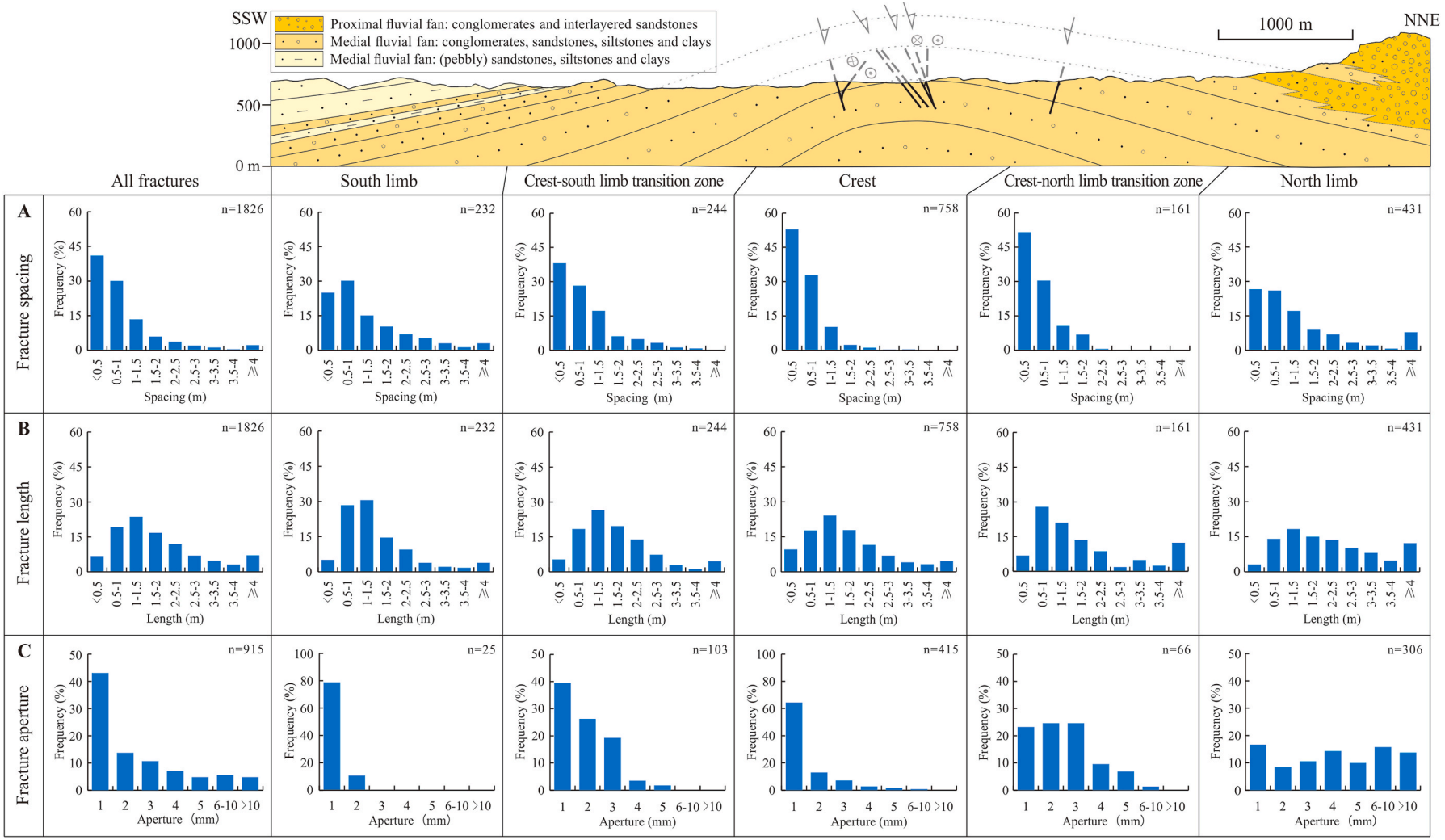

Fig. 4. Distribution of (A) fracture spacing, (B) length and (C) aperture in different structural positions. The cross section of the Puig-reig anticline is modified from Cruset et al. (2016).

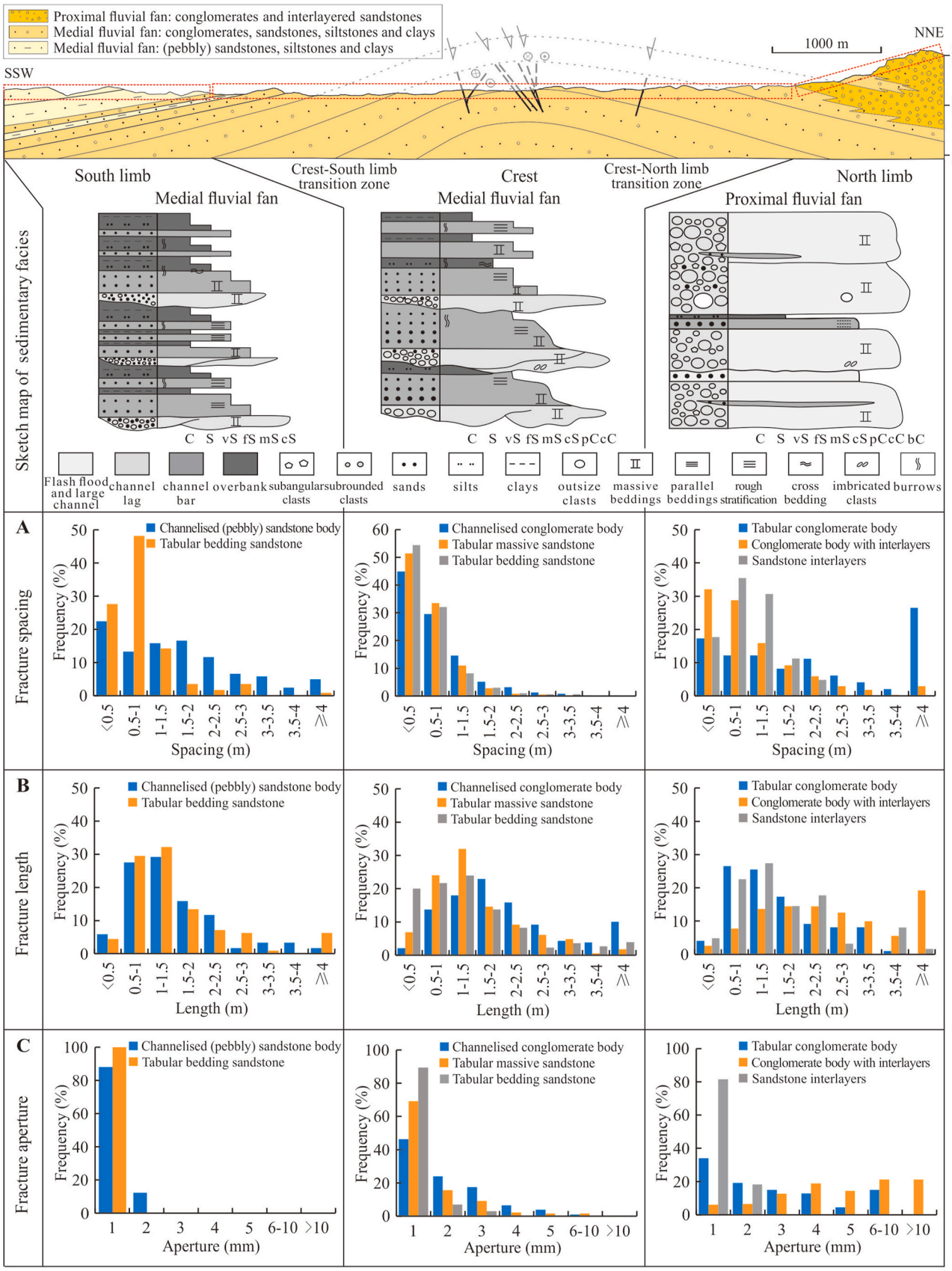

Fig. 5. Distribution of fracture (A) spacing, (B) length and (C) aperture for typical lithofacies in different sedimentary facies (proximal to medial fluvial fan). The cross section of the Puig-reig anticline is modified from Cruset et al. (2016).

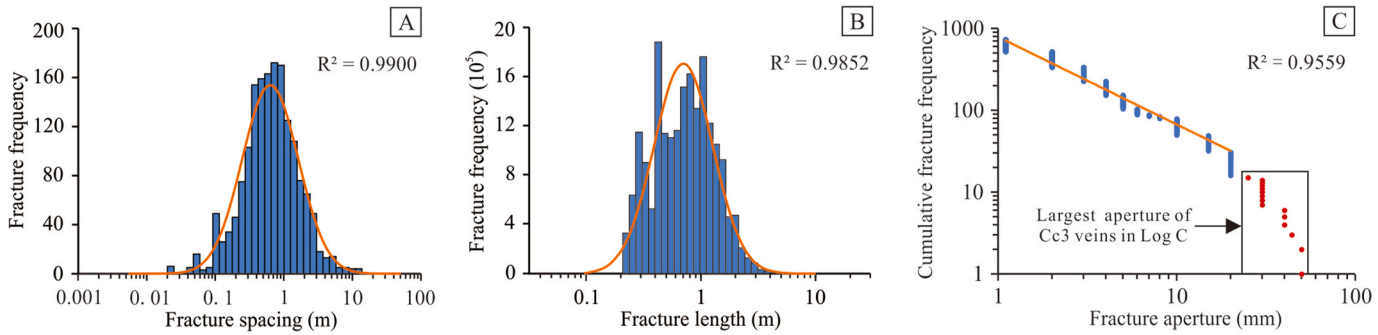

Fig. 6. Distributions of fracture attributes: (A) log-normal distribution of fracture spacing; (B) log-normal distribution of fracture length including correction for size bias with respect to the longest fracture; (C) power law distribution of fracture aperture. Note the logarithmic scales of the *X* axes in (A) and (B) and of both axes in (C).

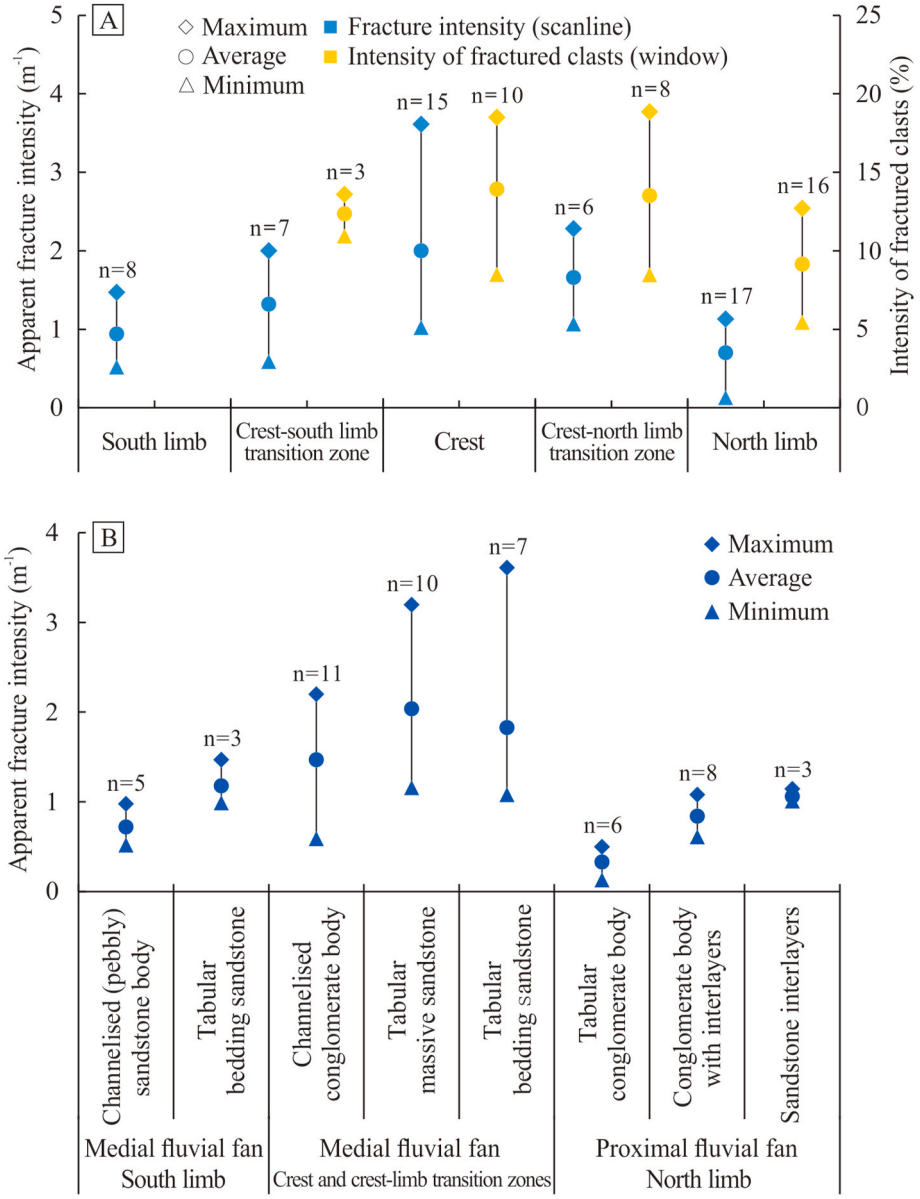

Fig. 7. (A) Apparent fracture intensity and intensity of fractured clasts of conglomerates in different structural positions, using the scanline and window fracture sampling methods, respectively. The window sampling was not used in the south limb due to the lack of conglomerate layers. (B) Apparent fracture intensity of typical lithofacies of different sedimentary facies (proximal to medial fluvial fan) in different structural positions. (*n* is the number of scanlines and windows).

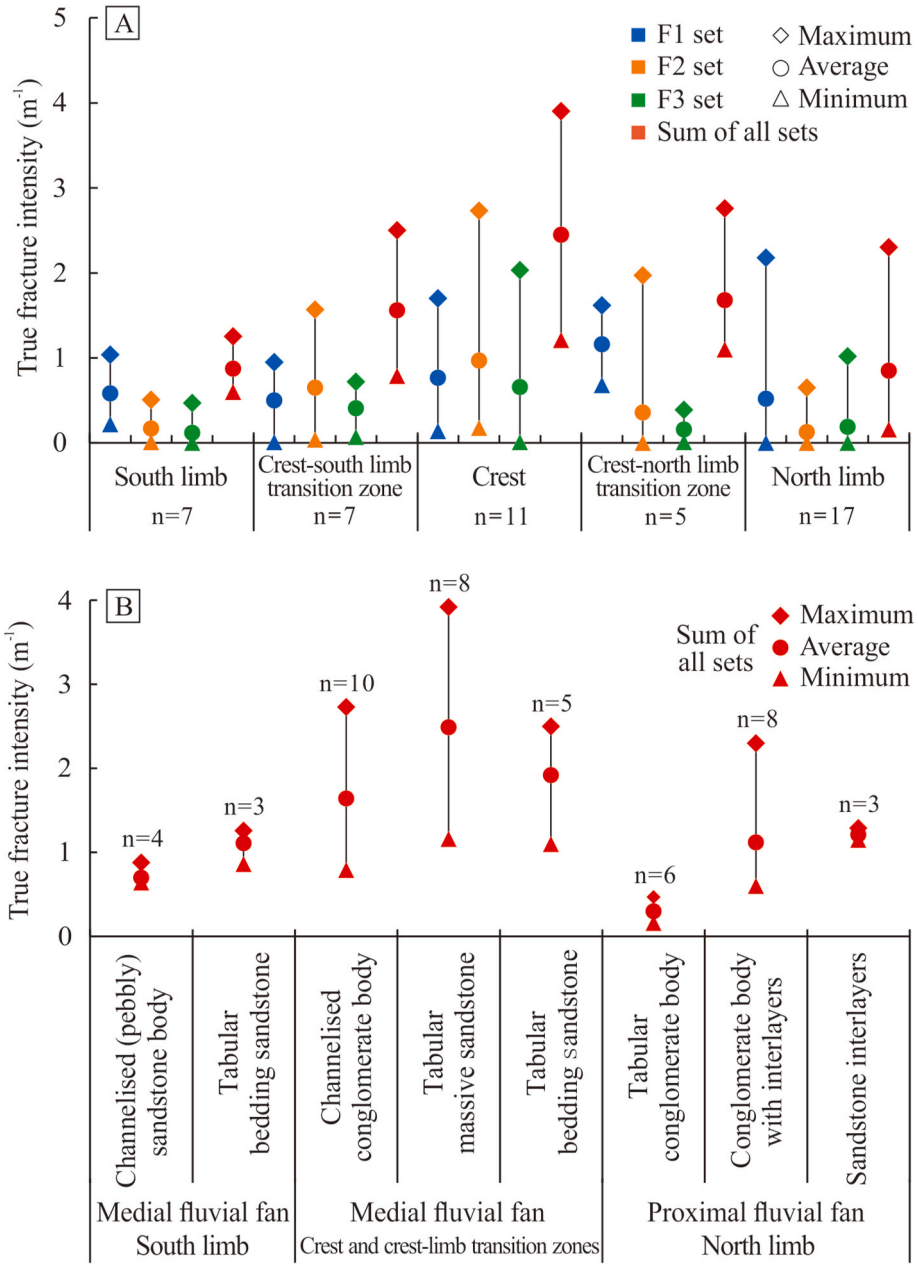

Fig. 8. (A) True fracture intensity of the F1, F2, F3 fracture sets in different structural positions, using the scanline sampling method. (B) True fracture intensity of typical lithofacies of different sedimentary facies (proximal to medial fluvial fan) in different structural positions. (*n* is the number of scanlines).

is the dominant one and is equivalent to the first generation of calcite cement identified by Cruset et al. (2016). Cc1 is the predominant cement filling fractures and interparticle pores throughout the Puig-reig anticline. Cc1 has bright orange cathodoluminescence and blocky or elongated crystal morphology with crystal size mainly ranging from 0.1 to 3 mm (Fig. 9A and B). Veins formed by multi-episodic crack-seal events are also occasionally observed (Fig. 9A and B). The second generation (Cc2) precipitated mainly in fractures and rarely in interparticle pores. Cc2 presents dull orange luminescence and blocky or elongated crystal morphology with slightly larger crystal sizes than Cc1, mainly ranging from 0.2 to 5 mm (Fig. 9C and D). The third (Cc3) and fourth (Cc4) cement generations only precipitated in fractures. Cc3 presents dull luminescence and euhedral blocky crystal morphology ranging in size from a few millimetres up to several centimetres (Fig. 9E and F). Cc4 is not luminescent and presents elongated crystal morphology or palisade structure made of bladed crystals with sizes generally smaller than 1 mm (Fig. 9G and H). This cement occasionally fills space originated by the reopening of veins hosting older cements (Fig. 9G and H).

5. Discussion

5.1. Controlling factors of fracture attributes

The fracture sets identified in the Puig-reig anticline present significant variation of their constituent attributes depending on their structural position within the anticline and the host facies (from the proximal to the medial fluvial fan). This section discusses how fracture network attributes vary across the different structural positions and sedimentary facies and thus identifies the controlling factors of fracture distribution in the Puig-reig anticline. Due to the lack of outcrops parallel to bedding, it is difficult to identify the terminations and relative cross-cutting relationships between the different fracture sets. Thus, systematically

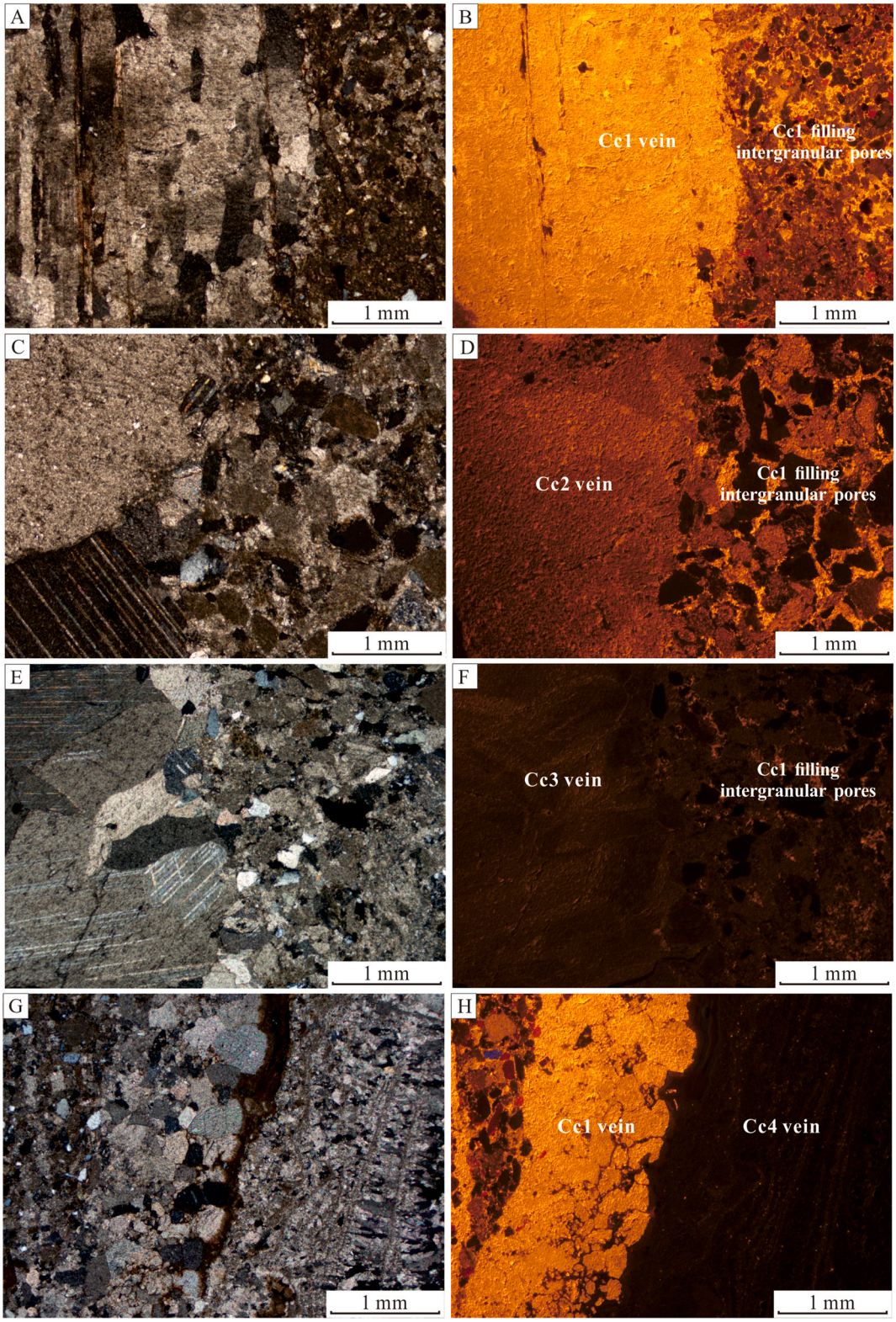

Fig. 9. Images of polarizing optical microscope (left) and cathodoluminescence (right) of calcite cements. (A–B) Cc1 calcite vein with homogeneous bright orange luminescence. (C–D) Cc2 calcite vein with duller luminescence than intergranular Cc1. (E–F) Cc3 calcite vein with duller luminescence than intergranular Cc1. (G–H) Fracture filled by Cc1 calcite vein was reopened and cemented by Cc4 calcite vein with black luminescence. (For interpretation of the references to colour in this figure legend, the reader is referred to the Web version of this article.)

establishing the chronology of the fracture sets and explaining the variation of fracture sets across the different structural positions are challenging tasks. Accordingly, we focus on the exploration of the distribution of fracture spacing, intensity, length and aperture, and the related controlling factors.

5.1.1. *Controlling factors of fracture spacing and intensity*

Fracture spacing presents a log-normal distribution, mainly ranging between 0.2 m and 1.2 m (Fig. 6A). However, the fracture spacing and intensity still vary significantly across the different structural positions (Figs. 4A, 7A and 8), with relatively smaller spacing and higher intensity in the crest, NTZ and STZ, and conversely, with relatively larger spacing and lower intensity in the south and north limbs. To determine the real relationship between fracture intensity and structural position, the effects of other potential controlling factors should be mitigated as much as possible. Thus, layers with same lithology and similar bedding thickness were chosen for comparison. Fig. 10A1-A2 show a clear negative correlation between fracture intensity and distance to the anticline hinge for conglomerate layers and sandstone layers, respectively, with fracture intensity decreasing significantly far from the anticline hinge. For folds developed according to the Tangential Longitudinal Strain model (TLS) (*e.g.*, Hudleston and Treagus, 2010), the fold hinge and nearby structural positions tend to experience more intensive fracturing due to their greater curvature and finite strain with respect to the limbs (Bellahsen et al., 2006; Iñigo et al., 2012; Awdal et al., 2013). If flexural slip was the dominant folding mechanism, then the thin and soft layers in limbs would be ones subjected to the highest strain. However, our field data better matches the first option because the anticline crest features more intensive fracturing than the limbs. Besides, a neutral line can divide a fold into an outer-arc extensional area and an inner-arc shortening area. Sets of layer-perpendicular extensional fractures are typical outer-arc extensional structures (Frehner, 2011). However, only a few normal faults developed in the crest of the Puig-reig anticline, which lacks systematic extensional fractures. Moreover, the analysis of Frehner (2011) reveals that when the fold is gentle (as in the case of the Puig-reig anticline) only a small area at the outer arc would undergo extension. These observations suggest that the anticline probably did not experience intensive outer arc extension.

Fracture intensity has been described to be closely related to the bedding thickness (Ladeira and Price, 1981). Some studies reported a

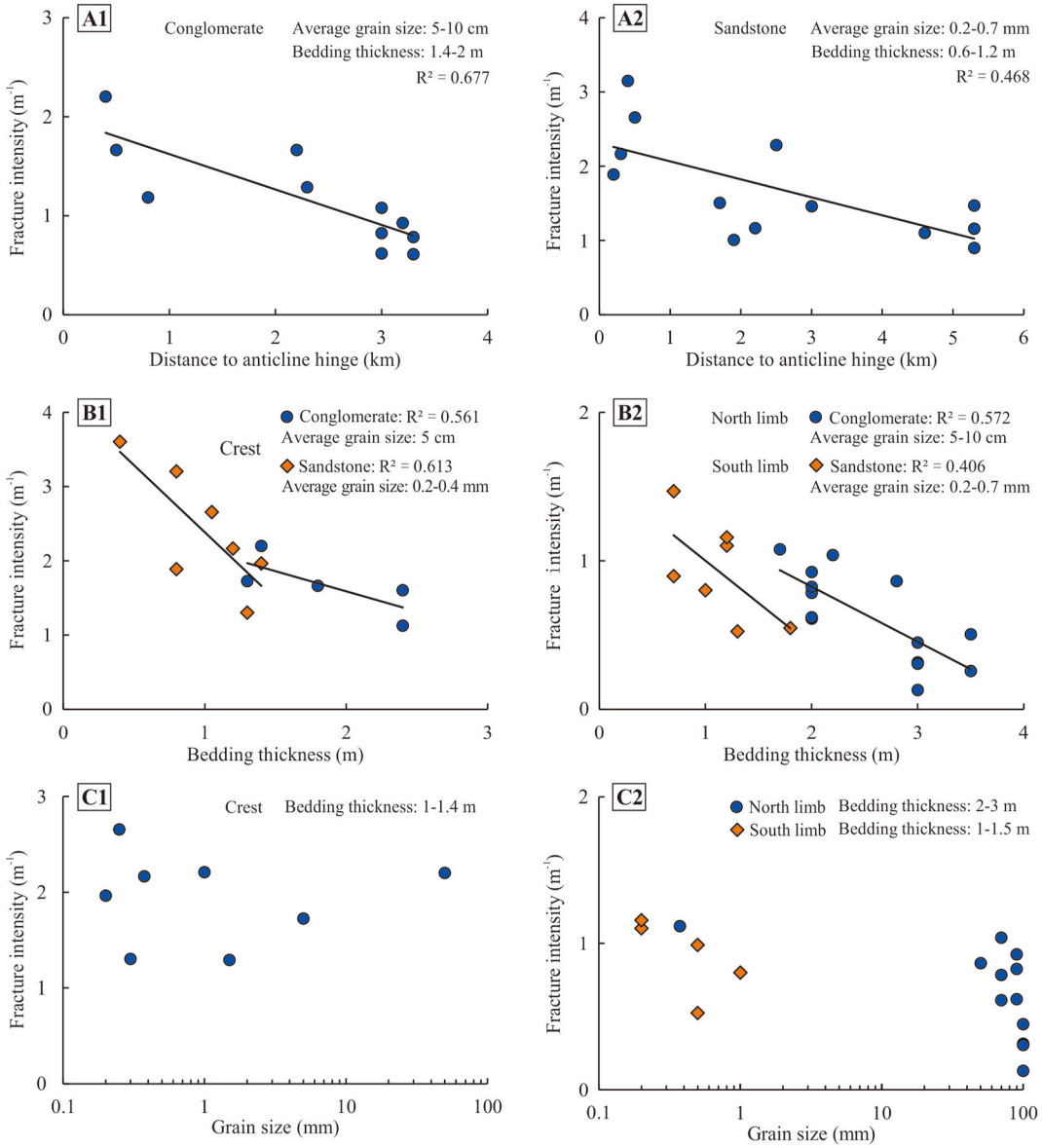

Fig. 10. Cross plots between fracture intensity and structural position and sedimentary characteristics. (A) Fracture intensity *vs.* distance to anticline hinge. (B) Fracture intensity *vs.* bedding thickness. (C) Fracture intensity *vs.* grain size.

clear negative correlation between fracture intensity and bedding thickness (Huang and Angelier, 1989; Florez-Niño et al., 2005; Wennberg et al., 2007). However, others did not reveal systematic relationships (Guiton et al., 2003; Ortega et al., 2010; Awdal et al., 2013). In this study layers with same lithology and located in the same structural position were chosen for comparison to determine the real relationship between fracture intensity and bedding thickness. Fig. 10B1 reveals a clear negative correlation between fracture intensity and bedding thickness for both conglomerate and sandstone layers in the anticline crest. Fig. 10 B2 shows a similar negative correlation for sandstone layers in the south limb and conglomerate layers in the north limb. Furthermore, conglomerate layers generally tend to be thicker than sandstone layers, thus resulting in lower fracture intensity for the same structural position, *e.g.*, in the anticline crest (Fig. 10B1). Moreover, fracture intensity decreases more significantly in sandstone layers compared to conglomerate layers. This can be observed from differences on the slope of the trend lines in Fig. 10B1 and B2.

The grain size of host rocks has been frequently considered as a critical factor controlling rock strength (Přikryl, 2001; Suorineni et al., 2009). Both physical experiments and numerical simulations have revealed that the strength of brittle rocks decreases with increasing grain size (Fredrich et al., 1990; Yu et al., 2018). Fracture intensity is generally related to the rock strength or brittleness, and is higher within the stronger and more brittle rocks (Nelson, 2001). Thus, coarse-grained rocks tend to present higher fracture intensity than fine-grained rocks, especially in carbonates (Hugman and Friedman, 1979; Hanks et al., 1997). However, a negative correlation between fracture intensity and grain size has also been reported in sandstones (Watkins et al., 2015a). In the present case, there also seems to be a subtle negative correlation between fracture intensity and grain size with relatively higher intensity in sandstone layers and lower intensity in coarse conglomerate layers. However, the variation of fracture intensity can be caused by other factors. There is not a clear relationship between fracture intensity and grain size when other factors, i.e., structural position and bedding thickness, are well controlled (Fig. 10C1 and C2). This indicates that grain size is not a significant factor controlling fracture intensity in the Puig-reig anticline, compared to the structural position or the bedding thickness.

In addition to the structural position, bedding thickness and grain size, here we explore the effect of lithological associations on fracture intensity. To mitigate the influence of other factors, the scanlines selected for comparison are those that correspond to layers with the same lithology, similar bedding thickness and that are located in same structural position. Fig. 11A presents three typical lithological associations in the anticline crest, where sandstone layers with multiple thin interlayers of fine sediments (Layer C-1) show relatively smaller fracture spacing than sandstone layers in between thick overbank fine deposits (Layer C-2) and those in between thick channel lag conglomerate bodies (Layer C-3). Similarly, Fig. 11B shows that sandstone layers with multiple interlayers of fine deposits (Layer S-1) present relatively smaller fracture spacing than those in between thick fine deposits (Layer S-2) in the south limb. In the north limb, Fig. 11C shows that conglomerate bodies with sandstone interlayers (Layer N-1) have smaller fracture spacing than other conglomerate bodies with a limited amount of sandstone lenses (Layer N-2). The high competence contrast at distinct mechanical stratigraphic positions (*e.g.*, at the interfaces between carbonate or sandstone layers and fine deposits) favours the development of joints or faults (Sibson, 1996; Wilkins et al., 2014). In this study, the interlayering between competent sandstone layers and thin incompetent fine deposits results in a high competence contrast, which favours the formation of fractures in the competent sandstone layers (*i.e.*, Layer C-1 and Layer S-1 in Fig. 11A and B). However, sandstone layers developed between thick incompetent fine deposits present relatively larger fracture spacing (Layer C-2 and Layer S-2 in Fig. 11A and B), compared to those with thin interlayers of fine deposits. This is probably because thick incompetent lithologies are capable of accommodating higher amount of pre-failure strain, *e.g.*, by means of inter-granular sliding, pressure solution, pore collapse and associated dewatering (Ferrill and Morris, 2008). Sandstone layers developed between thick conglomerate bodies (Layer C-3 in Fig. 11A) also present relatively larger fracture spacing. This is mainly because the competence contrast between competent sandstones and conglomerates is lower than that between competent sandstones and incompetent fine deposits. The competence contrast of interlayered conglomerate and sandstone layers in the north limb is higher than that of conglomerate layers with limited sandstone lens.

Based on the above analysis, we can conclude that fracture intensity is controlled by the structural position, bedding thickness and lithological associations, while the host rock's grain size only has a limited effect on fracture intensity. To quantitatively compare the relative importance of each factor for controlling fracture intensity, multiple linear regression analysis using SPSS software (IBM Corp, 2017) was employed in this study. First, lithological associations were classified and digitalised based on their effects on fracture intensity. The lithological association of competent layers with multiple thin incompetent layers (*e.g.*, Layer C-1 and Layer S-1 in Fig. 10) is assigned a value of 1 because it is conducive to the development of fractures. The lithological association of competent layers between thick incompetent layers (*e.g.*, Layer C-2 and Layer S-2 in Fig. 10) and the lithological association of interlayered competent conglomerate and sandstone layers (*e.g.*, Layer C-3 and Layer N-1 in Fig. 10) are assigned a value of 2. The lithological association of competent conglomerate layers with limited sandstone lens is assigned a value of 3, because it is not favourable for the development of fractures. Then, a multiple linear regression equation for fracture intensity can be used:

$$X_n = \frac{X - \overline{X}}{X_{max} - X_{min}} \tag{1a}$$

$$I_n = c_1 \times P_1 + c_2 \times P_2 + c_3 \times P_3 + c_4 \times P_4 \tag{2}$$

where, X, X_n, $\overline{X}$, $X_{\max}$ and $X_{\min}$ are the actual, normalised, average, maximum and minimum values for each parameter, respectively, I_n is the normalised fracture intensity, P_1 to P_4 are the normalised influence factors on fracture intensity, of structural position (distance to the anticline hinge), bedding thickness, lithological association, and lithology (grain size), respectively, and c_1 to c_4 are the standardised regression coefficients of the four influence factors, respectively. Finally, the relative importance of each factor for controlling fracture intensity can be determined based on the standardised regression coefficient of each factor. The data of 53 scanlines reached the following multiple linear regression equation:

$$I_n = -0.509 \times P_1 - 0.325 \times P_2 - 0.252 \times P_3 + 0.07 \times P_4 \quad (R^2 = 0.636) \tag{3}$$

Thus, this analysis confirms the qualitative observations that fracture intensity is mainly controlled by the structural position and is also moderately affected by bedding thickness and lithological associations, while the host rock's grain size has a very limited effect on fracture intensity.

5.1.2. Controlling factors of fracture length and aperture

Data displayed on Fig. 12A1 and A2 show positive correlations between fracture length and bedding thickness, for conglomerate and sandstone layers in the anticline crest and sandstone layers in the south limb of the anticline. Furthermore, fracture length is approximately equal to the bedding thickness in these cases. On the other hand, the fracture length of many conglomerate layers is larger than the bedding thickness in the north limb, while some thick conglomerate layers present anomalous small fracture lengths (Fig. 12A2). These anomalous values correspond to the tabular conglomerate bodies in the northwest zone of the anticline. The limited outcrop size in this area can exert an

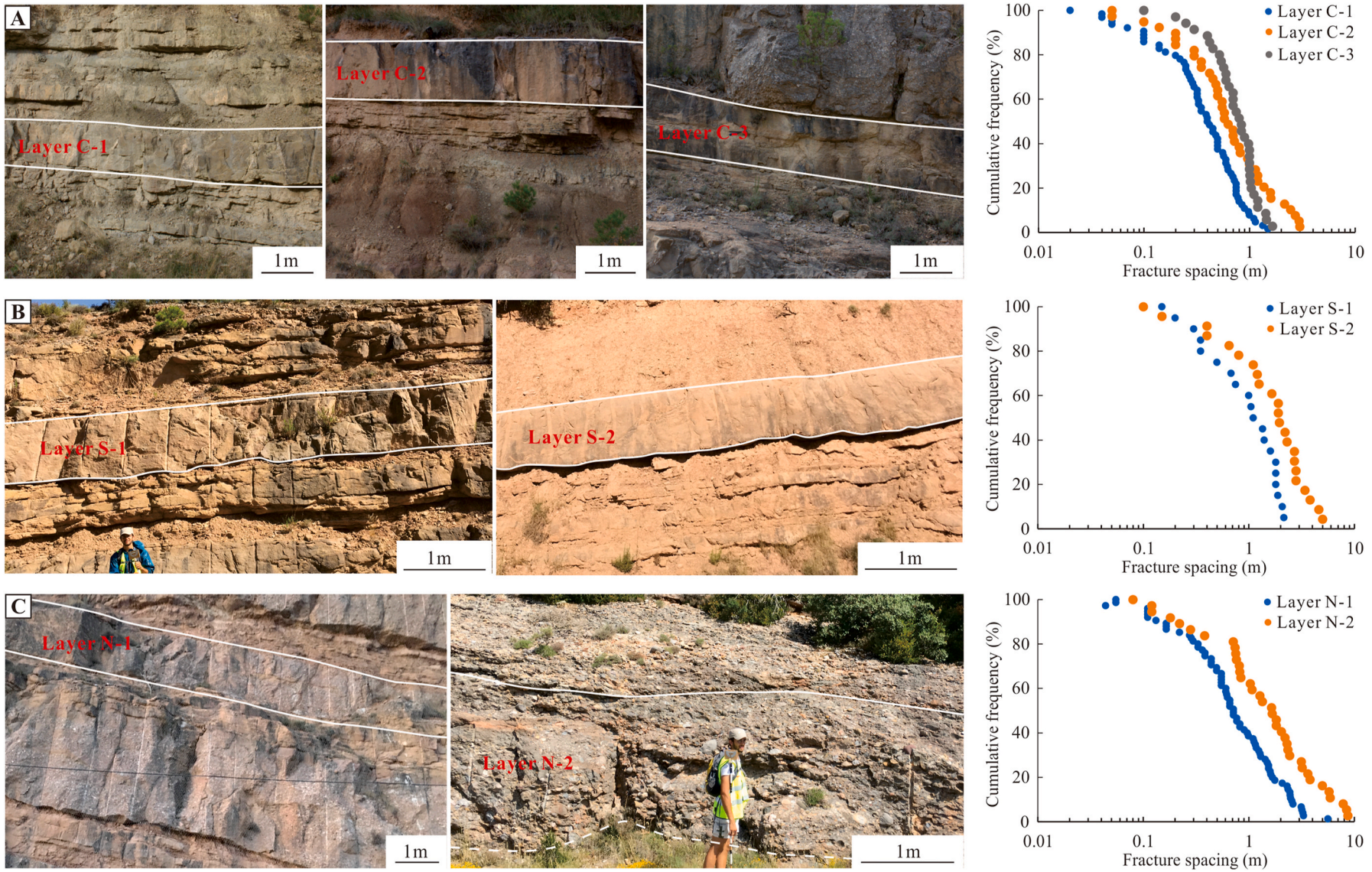

Fig. 11. Typical lithological associations in different sedimentary facies and their cumulative distributions of fracture spacing. (A) Massive sandstones with multiple interlayers of fine deposits (Layer C-1), massive sandstones between thick fine deposits (Layer C-2), and massive sandstones between thick conglomerate bodies (Layer C-3) in the anticline crest. (B) Massive sandstones with multiple interlayers of fine deposits (Layer S-1) and massive sandstones between thick fine deposits (Layer S-2) in the south limb. (B) Conglomerate bodies with stable sandstone interlayers (Layer N-1) and conglomerate bodies with limited sandstone lens (Layer N-2) in the north limb.

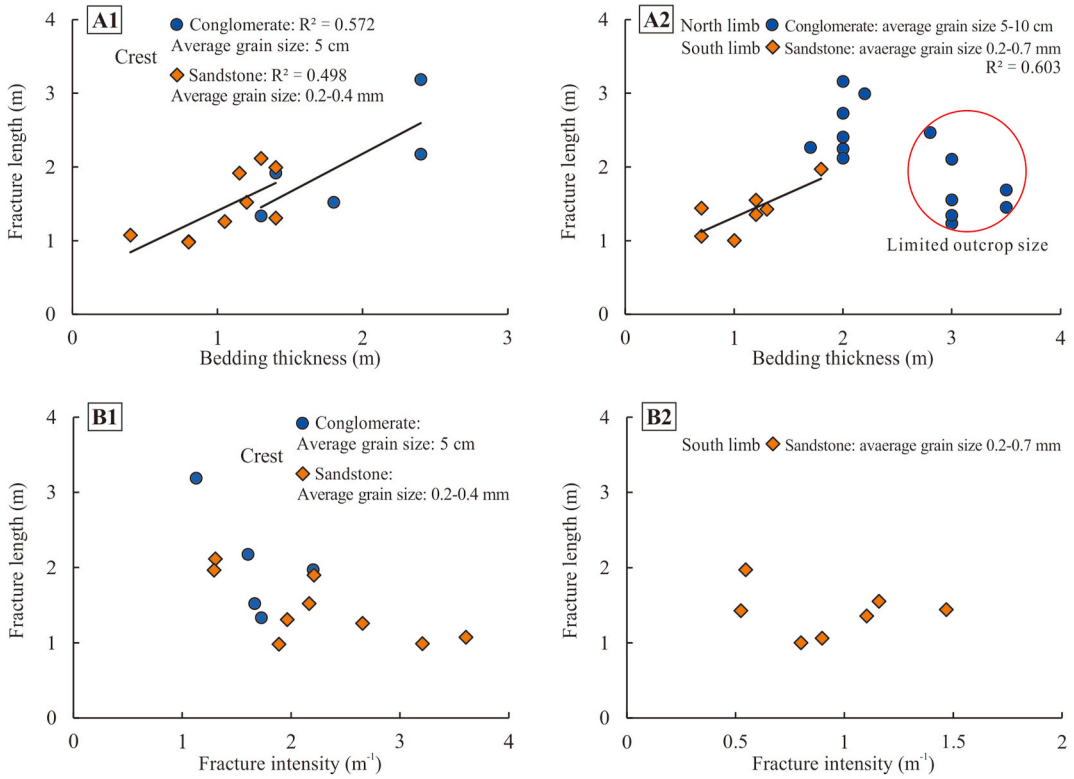

Fig. 12. (A1-A2) Cross plots between fracture length and bedding thickness. (B1–B2) Cross plots between fracture length and fracture intensity.

important effect on the collected data of fracture length due to the so-called 'censoring bias' (Zeeb et al., 2013a).

The types of fracture intersections with bedding interfaces are significantly affected by their strength. Fracture terminations are more likely to occur at very weak bedding interfaces between competent and incompetent layers, such as at interfaces between sandstone and clay, whereas strong bedding interfaces that put in contact competent layers favour fracture propagation across the interfaces (Cooke and Underwood, 2001). In the crest, crest-limb transition zones and south limb, where interbedding of conglomerates or sandstones and clays are common in the medial fluvial fan, more fractures tend to abut at the weak bedding interfaces. In this case, the fracture length is limited by the bedding thickness when fractures are stratabound (Wennberg et al., 2006). The fine deposits f the north limb are very sparse in the proximal fluvial fan, commonly resulting in strong contacts between adjacent conglomerate bodies or between conglomerates and sandstones. These relatively strong bedding interfaces in the proximal fluvial fan may promote the propagation of some long fractures but fewer facture population.

In addition, the fracture length may be structurally controlled and tend to be larger in higher strained zones to accommodate deformation during folding. For instance, Ghosh and Mitra (2009) calculated greater average fracture lengths in hinge zones compared to fold limbs. However, in the present case, the relatively higher strained crest corresponds to relatively higher fracture intensity but not larger fracture lengths. Besides, there is no clear correlation between the fracture length and intensity when other factors, *i.e.*, structural position and lithology, are well constrained (Fig. 12B1 and B2). Therefore, for the case study, the fracture length is not significantly affected by the structural position.

In the Puig-reig anticline, fracture apertures are generally smaller than 2 mm, while relatively larger values are mainly concentrated in conglomerate layers (Fig. 5C). This indicates that the sedimentary and diagenetic characteristics of the host rocks are the main controlling factor in terms of apertures rather than their structural position. This observation differs from some previous studies that suggested that wide apertures may be expected in high-strain zones (Jamison, 1997), *e.g.*, fracture apertures widen from the low-strain backlimb to the high-strain hinge (Iñigo et al., 2012). However, there is no clear correlation between fracture aperture and fracture intensity in this study (Fig. 13A), but we observe a subtle positive correlation between fracture aperture and length (Fig. 13B). This is consistent with other studies that reported that longer fractures tend to present wider apertures (Vermilye and Scholz, 1995; Olson, 2003; Ellis et al., 2012). We interpret this as an indication that these thick and massive conglomerate layers are not easily fractured, and thus strain tends to be accommodated by lengthening, widening and reopening of existing fractures rather than by developing new ones, thus resulting in larger fracture length and aperture but lower fracture intensity. The large aperture and prevalent calcite veins in conglomerate bodies are discussed in section 5.2.

5.1.3. *Fracture patterns in the Puig-reig anticline*

Based on the above analysis, Fig. 14 shows a schematic diagram that summarises the main fracture patterns of the Puig-reig anticline. The crest of the anticline, which is dominated by medial fluvial deposits (conglomerates, sandstones and clays), presents relatively high fracture intensity and variable fracture length and aperture. The north limb, which is dominated by proximal fluvial deposits (conglomerates and sandstones), presents relatively low fracture intensity but large fracture length and aperture. The south limb, dominated by medial fluvial deposits (sandstones and clays), presents relatively low fracture intensity and small length and aperture. The NTZ and STZ of the anticline feature variable fracture length and aperture and intermediate fracture intensity between the anticline crest and limbs. Fracture intensity is mainly controlled by the structural position, bedding thickness and lithological associations. Fracture length and aperture are mainly controlled by the host rock's sedimentary characteristics, while the structural position has a limited effect on them. Fracture length is mainly controlled by bedding thickness and affected by lithological associations. Fracture aperture is mainly controlled by lithology, with relatively larger values developed in conglomerate layers.

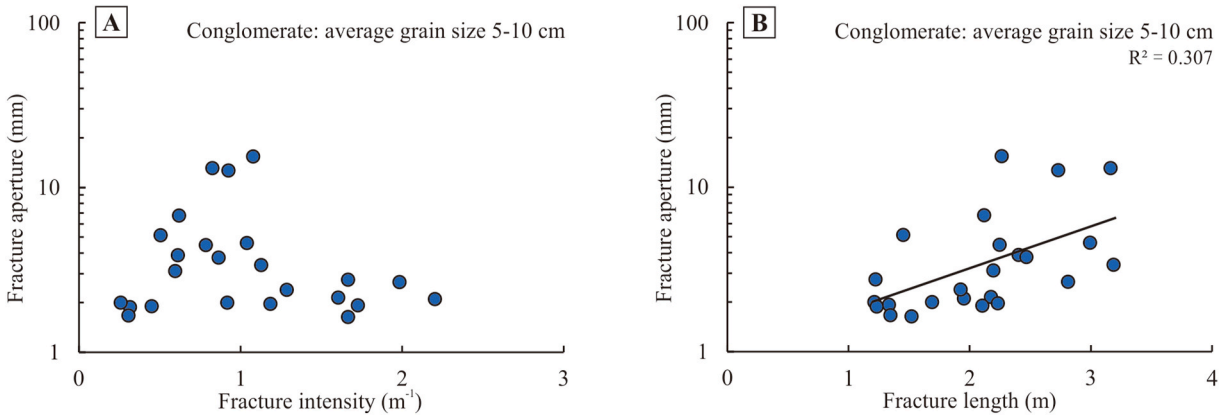

Fig. 13. (A) Cross plot between fracture aperture and fracture intensity. (B) Cross plots between fracture aperture and fracture length.

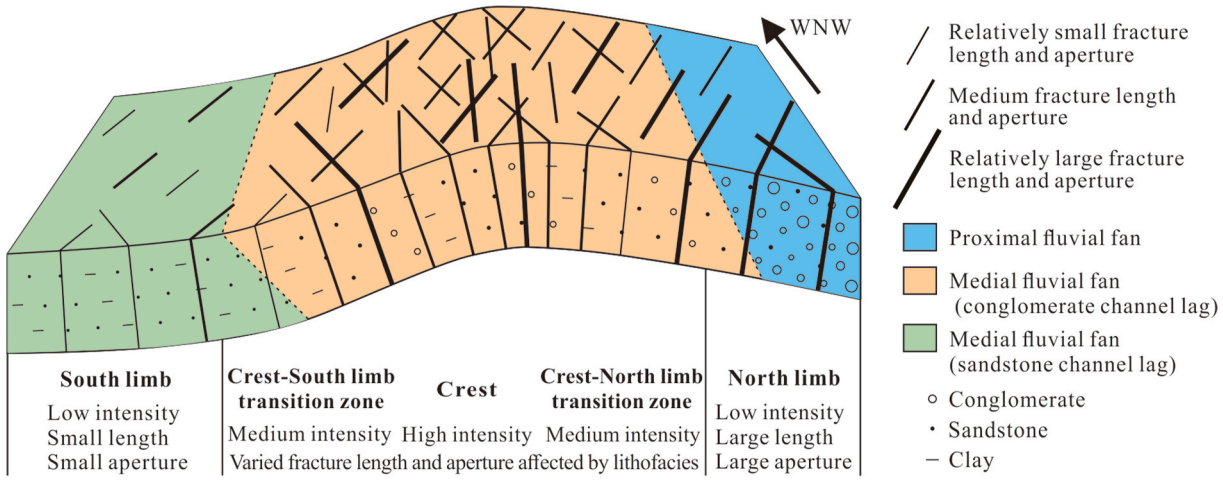

Fig. 14. Schematic diagram of fracture distribution across different structural positions and sedimentary facies. Note: the diagram does not show the termination relations between different fracture sets due to the lack of outcrops parallel to bedding planes to determine them.

5.2. Rock fracturing and vein formation

Fractures can potentially act as conduits for fluid flow and as depositional sites for cement precipitation. Therefore, fracture-filling cements are very useful to understand the conditions in which precipitation took place, including stress, strain, pressure, temperature, fluid composition and fluid origin during vein growth (Bons et al., 2012, and references therein). Structures and microstructures of calcite veins can be used to reveal fracture spatial and temporal distributions and also the fracturing and filling process in different structural positions and rock units (Gomez-Rivas et al., 2014). In the Puig-reig anticline, fractures are filled by four generations of calcite (Cc1 to Cc4) that formed veins (Fig. 8). Among these, Cc1 is the dominant generation, and is related to fluid flow during the anticline growth (Cruset et al., 2016). The clumped isotope thermometry data presented by these authors indicate that Cc1 precipitated from fluids at 92 °C to 129 °C. These temperatures are greater than the maximum temperatures reached by the Berga and Solsona strata during burial according to the maximum burial of 1.7 km and a geothermal gradient of 25 °C/km, indicating the input of external hydrothermal fluids. Besides, most Cc1 veins present a syntaxial microstructure with blocky calcite growing from the vein wall to the centre. Syntaxial veins with strong growth competition, formed by crystal growth into fracture porosity, are compatible with advective transport of fluid along fractures and fracture networks (Bons et al., 2012). Thus, fractures acted both as conduits for fluid flow and as depositional sites for calcite precipitation in the Puig-reig anticline during fold growth. More samples and geochemical data are required in order to carry out a more systematic study to reveal the origin of calcite cement and the temporal and spatial relationships between calcite cementation, fluid flow and fracture development. However, this is beyond the scope of the present study.

As discussed in section 5.1, the lower fracture intensity in the north limb is likely caused by its larger bedding thickness and lower strain compared to the crest, NTZ and STZ. When strain is high enough to cause brittle failure, fewer fractures develop in thick conglomerate bodies compared to sandstone layers. Besides, strain can also be accommodated by the cracking of clasts in conglomerates. Progressive stretching caused by folding can be accommodated by the propagation and/or re-opening and widening of previous fractures or by the formation of new ones (Watkins et al., 2015a). Strain accommodation by fracture propagation versus new fracture nucleation depends on the rock strength in a way that propagation rates decrease with increasing ductility (*e.g.*, Gomez-Rivas et al., 2015). Moreover, layer rotation (*e.g.*, due to folding), as well as mechanical anisotropy, can also reduce the fracture propagation rate (Gomez-Rivas and Griera, 2012). Eberhardt et al. (1999) found that longer grain boundaries and larger intergranular cracks, resulting from increasing grain size, provide longer paths of weakness for growing cracks to propagate along. This in turn promotes a reduction of the rock strength once the longer cracks begin to coalesce and interact. The propagation, re-opening and widening of existing fractures and the formation of new ones can operate at the same time in all structural positions and lithofacies. However, we observe that it is difficult to form

many new fractures to accommodate strain in the north limb due to the relatively lower strain in this structural position and the higher strength of these thick conglomerate bodies. Moreover, the existing fractures and veins in these thick conglomerate bodies act as weak parts compared to the host rock with high strength. Thus, the propagation, re-opening and widening of the existing fractures can accommodate strain when it is not high enough to form many new fractures. As a result, the conglomerate bodies in the north limb present relatively larger fracture length and aperture but lower intensity (Fig. 5). Besides, the re-opening or widening of existing fractures can also be proved by the observed multi-episodic crack-seal structure (Fig. 9A and B). Similarly, in the medial fluvial fan in the crest, NTZ and STZ, the channelised conglomerate bodies also present longer fractures with wider veins than those of sandstone layers.

5.3. Implications for reservoir potential

Fracture networks have a significant impact on reservoir performance. They can play a fundamental role in both controlling fluid migration and reservoir quality, especially in low-permeability and tight reservoirs in foreland fold-and-thrust belts (Casini et al., 2011; Wang et al., 2020). However, systematic fracture assessment in subsurface rocks is limited by the difficulty of sampling subseismic-scale fractures and because large fractures have much larger dimensions than that of the accessible rock volumes in boreholes (Ortega et al., 2006; Iñigo et al., 2012). Thus, a common strategy is to use outcrop analogues to understand the controlling factors of fracture networks and reduce uncertainty of subsurface predictions (Sanderson, 2016; Miranda et al., 2018). In the Pug-reig anticline, the distribution of fracture networks is significantly affected by the structural position and the host rock sedimentary characteristics, including bedding thickness, lithology and lithological associations. Although many fractures are sealed by calcite cement, this anticline can still be used as a reservoir analogue to explore the fracture distribution pattern and reservoir potential in folded clastic sediments, especially in the research context that fracturing in siliciclastic thrust belts is much less well documented than that in carbonate ones. The fluvial deposits present very low matrix porosity due to prevailing calcite cements, generally ranging from 0 to 4%. Among conglomerate and sandstone layers, only medium to coarse sandstones in the medial fluvial fan tend to present relatively high porosity (2.8% on average). Fracture intensity is mainly affected by structural position and sedimentary characteristics, with the relatively high values developing in the sandstone layers of the medial fluvial fan in the crest, NTZ and STZ of the anticline. The results indicate that the channel filling sandstone deposits, especially in the high strain zones, present relatively higher potential to be effective reservoirs.

6. Conclusions

The Puig-reig anticline, located in the south-eastern Pyrenean fold-and-thrust belt, is an excellent example of a folded fluvial depositional system, which exposes deposits of different sedimentary facies from the north limb to the south limb. A linear scanline method has been used to systematically collect fracture data, allowing the investigation of fracture distributions and their depositional and structural controlling factors. We reach the following conclusions:

(1) Four main sets of fractures have been identified, i.e., the NNW-SSE, ENE-WSW, WNW-ESE and NNE-SSW sets.
(2) Fracture attributes are strongly influenced both by their position within the fold and by the depositional characteristics of the sediments. Based on multiple linear regression analysis, fracture intensity is mainly controlled by the structural position, the bedding thickness and lithological associations, while grain size has a very limited effect on fracture intensity. Fracture length is mainly controlled by the bedding thickness and is affected by lithological associations. Fracture aperture is mainly controlled by lithology, with relatively larger values developed in conglomerate layers.
(3) Thick and massive conglomerate bodies can accommodate strain by the propagation and re-opening of existing fractures rather than by the formation of new fractures during fold growth, especially in the proximal fluvial fan in the north limb where strain was not high enough to promote the formation of a significant number of new fractures. Thus, compared to thin sandstone layers, conglomerate bodies tend to present relatively low fracture intensity but large fracture length and aperture.
(4) The study of the Puig-reig anticline reveals the fracture pattern in a folded fluvial succession, and provides an analogue case study for the prediction of subsurface fractured reservoirs with low matrix quality in fold-and-thrust belts.

Declaration of competing interest

The authors declare that they have no known competing financial interests or personal relationships that could have appeared to influence the work reported in this paper.

Acknowledgements

Funding was provided by the Catalan Council to the Grup Consolidat de Recerca “Geologia Sedimentària” (2017SGR-824) and the DGICYT Spanish Project PGC 2018-093903-B-C22 (Ministerio de Ciencia, Innovación y Universidades/Agencia Estatal de Investigación/Fondo Europeo de Desarrollo Regional, Unión Europea). XS acknowledges funding by the China Scholarship Council for a PhD scholarship (201806450043). EGR acknowledges funding provided by the Spanish Ministry of Science, Innovation and Universities (“Ramón y Cajal” fellowship RYC 2018-026335-I). JA is funded by MICINN (Juan de la Cierva fellowship - IJC 2018-036074-I). We thank associate editor Nicolas E. Beaudoin and two anonymous reviewers for their valuable suggestions, which have significantly improved this article.

References

Andrews, B.J., Roberts, J.J., Shipton, Z.K., Bigi, S., Tartarello, M.C., Johnson, G., 2019. How do we see fractures? Quantifying subjective bias in fracture data collection. Solid Earth 10, 487–516.
Arenas, C., Millán, H., Pardo, G., Pocoví, A., 2001. Ebro Basin continetal sedimentation associated with late compressional Pyrenean tectonics (North-Eastern Iberia): controls on basin margin fans and fluvial systems. Basin Res. 13, 65–89.
Awdal, A.H., Braathen, A., Wennberg, O.P., Sherwani, G.H., 2013. The characteristics of fracture networks in the shiranish formation of the bina bawi anticline; comparison with the Taq Taq field, Zagros, Kurdistan, NE Iraq. Petrol. Geosci. 19, 139–155.
Barbier, M., Hamon, Y., Callot, J.P., Floquet, M., Daniel, J.M., 2012. Sedimentary and diagenetic controls on the multiscale fracturing pattern of a carbonate reservoir: the Madison Formation (Sheep Mountain, Wyoming, USA). Mar. Petrol. Geol. 29, 50–67.
Barrier, L., Proust, J.N., Nalpas, T., Robin, C., Guillocheau, F., 2010. Control of alluvial sedimentation at foreland-basin active margins: a case study from the northeastern Ebro Basin (southeastern Pyrenees, Spain). J. Sediment. Res. 80, 728–749.
Beaudoin, N., Huyghe, D., Bellahsen, N., Lacombe, O., Emmanuel, L., Mouthereau, F., Ouanhnon, L., 2015. Fluid systems and fracture development during syn-depositional fold growth: an example from the Pico del Aguila anticline, Sierras Exteriores, southern Pyrenees, Spain. J. Struct. Geol. 70, 23–38.
Bellahsen, N., Fiore, P., Pollard, D.D., 2006. From spatial variation of fracture patterns to fold kinematics: a geomechanical approach. Geophys. Res. Lett. 33, 1–4.
Bergbauer, S., Pollard, D.D., 2004. A new conceptual fold-fracture model including prefolding joints, based on the Emigrant Gap anticline, Wyoming. Bull. Geol. Soc. Am. 116, 294–307.
Bons, P.D., Elburg, M.A., Gomez-Rivas, E., 2012. A review of the formation of tectonic veins and their microstructures. J. Struct. Geol. 43, 33–62.
Carrigan, J.H., Anastasio, D.J., Kodama, K.P., Parés, J.M., 2016. Fault-related fold kinematics recorded by terrestrial growth strata, Sant Llorenç de Morunys, Pyrenees Mountains, NE Spain. J. Struct. Geol. 91, 161–176.
Casini, G., Gillespie, P.A., Vergés, J., Romaire, I., Fernández, N., Casciello, E., Saura, E., Mehl, C., Homke, S., Embry, J.C., Aghajari, L., Hunt, D.W., 2011. Sub-seismic fractures in foreland fold and thrust belts: insight from the Lurestan Province, Zagros mountains, Iran. Petrol. Geosci. 17, 363–282.
Choukroune, P., 1989. The Ecors Pyrenean deep seismic profile reflection data and the overall structure of an orogenic belt. Tectonics 8, 23–39.

Cooke, M.L., Underwood, C.A., 2001. Fracture termination and step-over at bedding interfaces due to frictional slip and interface opening. J. Struct. Geol. 23, 223–238.
Cooper, S.P., Goodwin, L.B., Lorenz, J.C., 2006. Fracture and fault patterns associated with basement-cored anticlines: the example of Teapot Dome, Wyoming. Am. Assoc. Petrol. Geol. Bull. 90, 1903–1920.
Costa, E., Garcés, M., López-Blanco, M., Beamud, E., Gómez-Paccard, M., Larrasoaña, J. C., 2010. Closing and continentalization of the South Pyrenean foreland basin (NE Spain): magnetochronological constraints. Basin Res. 22, 904–917.
Cruset, D., Cantarero, I., Benedicto, A., John, C.M., Vergés, J., Albert, R., Gerdes, A., Travé, A., 2020. From hydroplastic to brittle deformation: controls on fluid flow in fold and thrust belts. Insights from the Lower Pedraforca thrust sheet (SE Pyrenees). Mar. Petrol. Geol. 120, 104517. https://doi.org/10.1016/j.marpetgeo.2020.104517.
Cruset, D., Cantarero, I., Travé, A., Vergés, J., John, C.M., 2016. Crestal graben fluid evolution during growth of the Puig-reig anticline (South Pyrenean fold and thrust belt). J. Geodyn. 101, 30–50.
Cruset, D., Cantarero, I., Vergés, J., John, C.M., Muñoz-López, D., Travé, A., 2018. Changes in fluid regime in syn-orogenic sediments during the growth of the south Pyrenean fold and thrust belt. Global Planet. Change 171, 207–224.
Del Santo, G., Garcia-Sansegundo, J., Sarasa, L., Torrebadella, J., 2000. Estratigrafía y estructura del Terciario en el sector oriental de la cuenca del Ebro entre Solsona y Manresa (NE de España). Rev. la Soc. Geológica España 13, 265–278 (in Spanish with English abstract).
Di Naccio, D., Boncio, P., Cirilli, S., Casaglia, F., Morettini, E., Lavecchia, G., Brozzetti, F., 2005. Role of mechanical stratigraphy on fracture development in carbonate reservoirs: insights from outcropping shallow water carbonates in the Umbria-Marche Apennines, Italy. J. Volcanol. Geoth. Res. 148, 98–115.
Eberhardt, E., Stimpson, B., Stead, D., 1999. Effects of grain size on the initiation and propagation thresholds of stress-induced brittle fractures. Rock Mech. Rock Eng. 32, 81–99.
Ellis, M.A., Laubach, S.E., Eichhubl, P., Olson, J.E., Hargrove, P., 2012. Fracture development and diagenesis of Torridon Group Applecross Formation, near an Teallach, NW Scotland: millennia of brittle deformation resilience? J. Geol. Soc. London. 169, 297–310.
Evans, M.A., Bebout, G.E., Brown, C.H., 2012. Changing fluid conditions during folding: an example from the central Appalachians. Tectonophysics 576–577, 99–115.
Evans, M.A., Fischer, M.P., 2012. On the distribution of fluids in folds: a review of controlling factors and processes. J. Struct. Geol. 44, 2–24.
Ferrill, D.A., Morris, A.P., 2008. Fault zone deformation controlled by carbonate mechanical stratigraphy , Balcones fault system , Texas. Am. Assoc. Petrol. Geol. Bull. 92, 359–380.
Fischer, M.P., Higuera-Díaz, I.C., Evans, M.A., Perry, E.C., Lefticariu, L., 2009. Fracture-controlled paleohydrology in a map-scale detachment fold: insights from the analysis of fluid inclusions in calcite and quartz veins. J. Struct. Geol. 31, 1490–1510.
Florez-Niño, J.M., Aydin, A., Mavko, G., Antonellini, M., Ayaviri, A., 2005. Fault and fracture systems in a fold and thrust belt: an example from Bolivia. Am. Assoc. Petrol. Geol. Bull. 89, 471–493.
Ford, M., Williams, E.A., Artoni, A., Vergés, J., Hardy, S., 1997. Progressive evolution of a fault-related fold pair from growth strata geometries, Sant Llorenç de Morunys, SE Pyrenees. J. Struct. Geol. 19, 413–441.
Fredrich, J.T., Evans, B., Wong, Teng-Fong, 1990. Effect of grain size on brittle and semibrittle strength: implications for micromechanical modelling of failure in compression. J. Geophys. Res. 95, 10907–10920.
Frehner, M., 2011. The neutral lines in buckle folds. J. Struct. Geol. 33, 1501–1508.
Ge, H., Jackson, M.P.A., Vendeville, B.C., 1997. Kinematics and dynamics of salt tectonics driven by progradation. Am. Assoc. Petrol. Geol. Bull. 81, 398–423.
Ghosh, K., Mitra, S., 2009. Structural controls of fracture orientations, intensity, and connectivity, Teton anticline, Sawtooth Range, Montana. Am. Assoc. Petrol. Geol. Bull. 93, 995–1014.
Gomez-Rivas, E., Bons, P.D., Koehn, D., Urai, J.L., Arndt, M., Virgo, S., Laurich, B., Zeeb, C., Stark, L., Blum, P., 2014. The Jabal Akhdar Dome in the Oman mountains: evolution of a dynamic fracture system. Am. J. Sci. 314, 1104–1139.
Gomez-Rivas, E., Griera, A., 2012. Shear fractures in anisotropic ductile materials: an experimental approach. J. Struct. Geol. 34, 61–76.
Gomez-Rivas, E., Griera, A., Llorens, M.G., 2015. Fracturing of ductile anisotropic multilayers: influence of material strength. Solid Earth 6, 497–514.
Guiton, M.L.E., Sassi, W., Leroy, Y.M., Gauthier, B.D.M., 2003. Mechanical constraints on the chronology of fracture activation in folded Devonian sandstone of the western Moroccan Anti-Atlas. J. Struct. Geol. 25, 1317–1330.
Gutmanis, J., Ardèvol i Oró, L., Díez-Canseco, D., Chebbihi, L., Awdal, A., Cook, A., 2018. Fracture analysis of outcrop analogues to support modelling of the subseismic domain in carbonate reservoirs, south-central Pyrenees. Geol. Soc. London, Spec. Publ. 459, 139–156.
Hanks, C.L., Lorenz, J., Teufel, L., Krumhardt, A.P., 1997. Lithologic and structural controls on natural fracture distribution and behavior within the Lisburne Group, northeastern Brooks Range and North Slope subsurface, Alaska. Am. Assoc. Petrol. Geol. Bull. 81, 1700–1720.
Healy, D., Rizzo, R.E., Cornwell, D.G., Farrell, N.J.C., Watkins, H., Timms, N.E., Gomez-Rivas, E., Smith, M., 2017. FracPaQ: a MATLAB™ toolbox for the quantification of fracture patterns. J. Struct. Geol. 95, 1–16.
Hennings, P.H., Olson, J.E., Thompson, L.B., 2000. Combining outcrop data and three-dimensional structural models to characterize fractured reservoirs: an example from Wyoming. Am. Assoc. Petrol. Geol. Bull. 84, 1–20.
Horton, B.K., Decelles, P.G., 2001. Modern and ancient fluvial megafans in the foreland basin system of the Central Andes, Southern Bolivia: implications for drainage network evolution if foldthrust belts. Basin Res. 13, 43–63.
Huang, Q., Angelier, J., 1989. Fracture spacing and its relation to bed thickness. Geol. Mag. 126, 355–362.
Hudleston, P.J., Treagus, S.H., 2010. Information from folds: a review. J. Struct. Geol. 32, 2042–2071.
Hugman, R.H.H., Friedman, M., 1979. Effects of texture and composition on mechanical behavior of experimentally deformed carbonate rocks. Am. Assoc. Petrol. Geol. Bull. 63, 1478–1489.
IBM Corp, 2017. IBM SPSS Statistics for Windows, Version 25.0. https://www.ibm.com/support/pages/downloading-ibm-spss-statistics-25.
Iñigo, J.F., Laubach, S.E., Hooker, J.N., 2012. Fracture abundance and patterns in the Subandean fold and thrust belt, Devonian Huamampampa Formation petroleum reservoirs and outcrops, Argentina and Bolivia. Mar. Petrol. Geol. 35, 201–218.
Institut Cartogràfic i Geològic de Catalunya, 2006. Regional Geological Map of Catalonia accessed 2.1.21). https://www.icgc.cat/en/Public-Administration-and-Enterprises/Downloads/Geological-and-geothematic-cartography/Geological-cartography/Geological-map-1-50-000/Regional-geological-map-of-Catalonia-1-50-000.
Instituto Geológico y Minero de España, 1977. Geophysical Information System accessed 10.1.20). http://info.igme.es/SIGEOF/#.
Instituto Geológico y Minero de España, 1995. Almacenamiento subterraneo de gas: previabilidad en formaciones detriticas y salinas accessed 3.20.21. http://info.igme.es/ConsultaSID/r.asp?IdDESCRIPTOR=2681.
Jamison, W.R., 1997. Quantitative evaluation of fractures on Monkshood anticline, a detachment fold in the foothills of western Canada. Am. Assoc. Petrol. Geol. Bull. 81, 1110–1132.
Jones, S.J., 2004. Tectonic controls on drainage evolution and development of terminal alluvial fans, southern Pyrenees, Spain. Terra. Nova 16, 121–127.
Lacroix, B., Baumgartner, L.P., Bouvier, A.S., Kempton, P.D., Vennemann, T., 2018. Multi fluid-flow record during episodic mode I opening: a microstructural and SIMS study (Cotiella Thrust Fault, Pyrenees). Earth Planet Sci. Lett. 503, 37–46.
Ladeira, F.L., Price, N.J., 1981. Relationship between fracture spacing and bed thickness. J. Struct. Geol. 3, 179–183.
Laubach, S.E., Olson, J.E., Cross, M.R., 2009. Mechanical and fracture stratigraphy. Am. Assoc. Petrol. Geol. Bull. 93, 1413–1426.
Lorenz, J.C., Cooper, S.P., Olsson, W.A., 2006. Natural fracture distributions in sinuous, channel-fill sandstones of the Cedar Mountain Formation, Utah. Am. Assoc. Petrol. Geol. Bull. 90, 1293–1308.
Mann, P., Gahagan, L., Gordon, M.B., 2003. Tectonic setting of the world's giant oil fields. In: Halbouty, M. (Ed.), Giant Oil and Gas Fields of the Decade 1990–1999, vol. 78. AAPG Memoir, pp. 15–105.
Martínez-Martínez, J.M., Soto, J.I., Balanyá, J.C., 2002. Orthogonal folding of extensional detachments: structure and origin of the Sierra Nevada elongated dome (Betics, SE Spain). Tectonics 21, 1–22.
Miranda, T.S., Santos, R.F., Barbosa, J.A., Gomes, I.F., Alencar, M.L., Correia, O.J., Falcão, T.C., Gale, J.F.W., Neumann, V.H., 2018. Quantifying aperture, spacing and fracture intensity in a carbonate reservoir analogue: crato Formation, NE Brazil. Mar. Petrol. Geol. 97, 556–567.
Muñoz-López, D., Alías, G., Cruset, D., Cantarero, I., John, C.M., Travé, A., 2020a. Influence of basement rocks on fluid evolution during multiphase deformation: the example of the Estamariu thrust in the Pyrenean Axial Zone. Solid Earth 11, 2257–2281.
Muñoz-López, D., Cruset, D., Cantarero, I., Benedicto, A., John, C.M., Travé, A., 2020b. Fluid dynamics in a thrust fault inferred from petrology and geochemistry of calcite veins: an example from the southern Pyrenees. Geofluids 2020 1–25.
Muñoz, J.A., 1992. Evolution of a continental collision belt: ECORS-Pyrenees crustal balanced cross-section. In: McClay, K.R. (Ed.), Thrust Tectonics. Springer, Dordrecht, pp. 235–246.
Nardini, N., Muñoz-López, D., Cruset, D., Cantarero, I., Martín-Martín, J., Benedicto, A., Gomez-Rivas, E., John, C., Travé, A., 2019. From early contraction to post-folding fluid evolution in the frontal part of the Bóixols thrust sheet (southern Pyrenees) as revealed by the texture and geochemistry of calcite cements. Minerals 9, 117.
Nelson, R.A., 2001. Geologic Analysis of Naturally Fractured Reservoirs. Gulf Professional Publishing, Houston.
Nelson, R.A., Serra, S., 1995. Vertical and lateral variations in fracture spacing in folded carbonate sections and its relation to locating horizontal wells. J. Can. Pet. Technol. 34, 51–56.
Ogata, K., Senger, K., Braathen, A., Tveranger, J., 2014. Fracture corridors as seal-bypass systems in siliciclastic reservoir-cap rock successions: field-based insights from the Jurassic Entrada Formation (SE Utah, USA). J. Struct. Geol. 66, 162–187.
Ogata, K., Storti, F., Balsamo, F., Tinterri, R., Bedogni, E., Fetter, M., Gomes, L., Hatushika, R., 2017. Sedimentary facies control on mechanical and fracture stratigraphy in turbidites. Bull. Geol. Soc. Am. 129, 76–92.
Olson, J.E., 2003. Sublinear scaling of fracture aperture versus length: an exception or the rule? J. Geophys. Res. Solid Earth 108, 2413.
Olson, J.E., Laubach, S.E., Lander, R.H., 2007. Combining diagenesis and mechanics to quantity fracture aperture distributions an fracture pattern permeability. Geol. Soc. Spec. Publ. 270, 101–116.
Ortega, O.J., Gale, J.F.W., Marrett, R., 2010. Quantifying diagenetic and stratigraphic controls on fracture intensity in platform carbonates: an example from the Sierra Madre Oriental, northeast Mexico. J. Struct. Geol. 32, 1943–1959.
Ortega, O.J., Marrett, R.A., Laubach, S.E., 2006. A scale-independent approach to fracture intensity and average spacing measurement. Am. Assoc. Petrol. Geol. Bull. 90, 193–208.
Peacock, D.C.P., 2001. The temporal relationship between joints and faults. J. Struct. Geol. 23, 329–341.
Peacock, D.C.P., Nixon, C.W., Rotevatn, A., Sanderson, D.J., Zuluaga, L.F., 2016. Glossary of fault and other fracture networks. J. Struct. Geol. 92, 12–29.

Přikryl, R., 2001. Some microstructural aspects of strength variation in rocks. Int. J. Rock Mech. Min. Sci. 38, 671–682.
Puigdefàbregas, C., Munñz, J.A., Marzo, M., 1986. Thrust belt development in the eastern Pyrenees and related depositional sequences in the southern foreland basin. In: Allen, P.A., Homewood, P. (Eds.), Foreland Basins. International Association of Sedimentologists Special Publication, pp. 229–246.
Puigdefàbregas, C., Muñoz, J.A., Vergés, J., 1992. Thrusting and foreland basin evolution in the Southern Pyrenees. In: McClay, K.R. (Ed.), Thrust Tectonics. Springer, Dordrecht, pp. 247–254.
Roure, F., Choukroune, P., Berastegui, X., Munoz, J.A., Villien, A., Matheron, P., Bareyt, M., Seguret, M., Camara, P., Deramond, J., 1989. Ecors deep seismic data and balanced cross sections: geometric constraints on the evolution of the Pyrenees. Tectonics 8, 41–50.
Sáez, A., Anadón, P., Herrero, M.J., Moscariello, A., 2007. Variable style of transition between Palaeogene fluvial fan and lacustrine systems, southern Pyrenean foreland, NE Spain. Sedimentology 54, 367–390.
Sanderson, D.J., 2016. Field-based structural studies as analogues to sub-surface reservoirs. Geol. Soc. Spec. Publ. 431, 207–217.
Serra-Kiel, J., Mató, E., Saula, E., Travé, A., Ferràndez-Canadell, C., Busquets, P., Samsó, J.M., Tosquella, J., Barnolas, A., Àlvarez-Pérez, G., Franquès, J., Romero, J., 2003a. An inventory of the marine and transitional middle/upper Eocene deposits of the southeastern pyrenean foreland basin (NE Spain). Geol. Acta 1, 201–229.
Serra-Kiel, J., Travé, A., Mató, E., Saula, E., Ferràndez-Canadell, C., Busquets, P., Tosquella, J., Vergés, J., 2003b. Marine and transitional Middle/Upper Eocene units of the southeastern pyrenean foreland basin (NE Spain). Geol. Acta 1, 177–200.
Shackleton, J.R., Cooke, M.L., Sussman, A.J., 2005. Evidence for temporally changing mechanical stratigraphy and effects on joint-network architecture. Geology 33, 101–104.
Sibson, R.H., 1996. Structural permeability of fluid-driven fault-fracture meshes. J. Struct. Geol. 18, 1031–1042.
Stephenson, B.J., Koopman, A., Hillgartner, H., McQuillan, H., Bourne, S., Noad, J.J., Rawnsley, K., 2007. Structural and stratigraphic controls on fold-related fracturing in the Zagros Mountain, Iran: implications for reservoir development. Geol. Soc. Spec. Publ. 270, 1–21.
Sun, X., Alcalde, J., Gomez-Rivas, E., Struth, L., Johnson, G., Travé, A., 2020. Appraisal of CO2 storage potential in compressional hydrocarbon-bearing basins: global assessment and case study in the Sichuan Basin (China). Geosci. Front. 11, 2309–2321.
Suorineni, F.T., Chinnasane, D.R., Kaiser, P.K., 2009. A procedure for determining rock-type specific hoek-brown brittle parameter s. Rock Mech. Rock Eng. 42, 849–881.
Suppe, J., Sàbat, F., Anton Muñoz, J., Poblet, J., Roca, E., Vergés, J., 1997. Bed-by-bed fold growth by kink-band migration: Sant llorenç de Morunys, eastern Pyrenees. J. Struct. Geol. 19, 443–461.
Taillefer, A., Soliva, R., Guillou-Frottier, L., Le Goff, E., Martin, G., Seranne, M., 2017. Fault-related controls on upward hydrothermal flow: an integrated geological study of the Têt fault system, eastern Pyrénées (France). Geofluids 2017 1–19.
Tavani, S., Granado, P., Corradetti, A., Seers, T., Casas, J.M., Muñoz, J.A., 2020. Transverse jointing in foreland fold-and-thrust belts: a remote sensing analysis in the eastern Pyrenees. Solid Earth 11, 1643–1651.
Tavani, S., Mencos, J., Bausà, J., Muñoz, J.A., 2011. The fracture pattern of the Sant Corneli Bóixols oblique inversion anticline (Spanish Pyrenees). J. Struct. Geol. 33, 1662–1680.
Terzaghi, R.D., 1965. Sources of error in joint surveys. Geotechnique 15, 287–304.
Travé, A., Calvet, F., Sans, M., Vergés, J., Thirlwall, M., 2000. Fluid history related to the Alpine compression at the margin of the south-Pyrenean Foreland basin: the El Guix anticline. Tectonophysics 321, 73–102.
Travé, A., Labaume, P., Vergés, J., 2007. Fluid systems in foreland fold-and-thrust belts: an overview from the southern Pyrenees. In: Lacombe, O., Lavé, J., Roure, F., Vergés, J. (Eds.), Thrust Belts and Foreland Basins. Springer, Berlin, Heidelberg, pp. 93–115.
Underwood, C.A., Cooke, M.L., Simo, J.A., Muldoon, M.A., 2003. Stratigraphic controls on vertical fracture patterns in Silurian dolomite, northeastern Wisconsin. Am. Assoc. Petrol. Geol. Bull. 87, 121–142.
Van Dijk, J.P., Bello, M., Toscano, C., Bersani, A., Nardon, S., 2000. Tectonic model and three-dimensional fracture network analysis of Monte Alpi (southern Apennines). Tectonophysics 324, 203–237.
Vergés, J., 1993. Estudi geològic del vessant sud del Pirineu oriental i central. Evolució cinemàtica en 3D. Ph.D. thesis. University of Barcelona, Barcelona (in Spanish).
Vergés, J., Marzo, M., Muñoz, J.A., 2002. Growth strata in foreland settings. Sediment. Geol. 146, 1–9.
Vergés, J., Marzo, M., Santaeulària, T., Serra-Kiel, J., Burbank, D.W., Muñoz, J.A., Giménez-Montsant, J., 1998. Quantified vertical motions and tectonic evolution of the SE Pyrenean foreland basin. Geol. Soc. London, Spec. Publ. 134, 107–134.
Vergés, J., Muñoz, J.A., Martínez, A., 1992. South Pyrenean fold and thrust belt: the role of foreland evaporitic levels in thrust geometry. In: K R, M. (Ed.), Thrust Tectonics. Springer, Dordrecht, pp. 255–264.
Vermilye, J.M., Scholz, C.H., 1995. Relation between vein length and aperture. J. Struct. Geol. 17, 423–434.
Wang, Z., Lü, X., Wang, S., Li, Y., Zhou, X., Quan, H., Li, R., 2020. Fracture systems and petrophysical properties of tight sandstone undergoing regional folding: a case study of the Cretaceous reservoirs in the Kuqa foreland thrust belt, Tarim Basin. Mar. Petrol. Geol. 111, 104055. https://doi.org/10.1016/j.marpetgeo.2019.104055.
Watkins, H., Butler, R.W.H., Bond, C.E., Healy, D., 2015a. Influence of structural position on fracture networks in the Torridon Group, Achnashellach fold and thrust belt, NW Scotland. J. Struct. Geol. 74, 64–80.
Watkins, H., Bond, C.E., Healy, D., Butler, R.W.H., 2015b. Appraisal of fracture sampling methods and a new workflow tocharacterise heterogeneous fracture networks at outcrop. J. Struct. Geol. 72, 67–82.
Wennberg, O.P., Azizzadeh, M., Aqrawi, A.A.M., Blanc, E., Brockbank, P., Lyslo, K.B., Pickard, N., Salem, L.D., Svånå, T., 2007. The Khaviz Anticline: an outcrop analogue to giant fractured Asmari Formation reservoirs in SW Iran. Geol. Soc. London, Spec. Publ. 270, 23–42.
Wennberg, O.P., Svånå, T., Azizzadeh, M., Aqrawi, A.M.M., Brockbank, P., Lyslo, K.B., Ogilvie, S., 2006. Fracture intensity vs. mechanical stratigraphy in platform top carbonates: the aquitanian of the asmari formation, Khaviz anticline, Zagros, SW Iran. Petrol. Geosci. 12, 235–246.
Wilkins, S., Mount, V., Mahon, K., Perry, A., Koenig, J., 2014. Characterization and development of subsurface fractures observed in the Marcellus Formation, Appalachian Plateau, north-central Pennsylvania. Am. Assoc. Petrol. Geol. Bull.
Williams, E.A., Ford, M., Vergés, J., Artoni, A., 1998. Alluvial gravel sedimentation in a contractional growth fold setting, Sant Llorenç de Morunys, southeastern Pyrenees. Geol. Soc. London, Spec. Publ. 134, 69–106.
Yu, Q., Zhu, W., Ranjith, P.G., Shao, S., 2018. Numerical simulation and interpretation of the grain size effect on rock strength. Geomech. Geophys. Geo-Energy Geo-Resour. 4, 157–173.
Yuste, A., Luzón, A., Bauluz, B., 2004. Provenance of Oligocene-Miocene alluvial and fluvial fans of the northern Ebro Basin (NE Spain): an XRD, petrographic and SEM study. Sediment. Geol. 172, 251–268.
Zeeb, C., Gomez-Rivas, E., Bons, P.D., Blum, P., 2013a. Evaluation of Sampling methods for fracture network characterization using Outcrops. Am. Assoc. Petrol. Geol. Bull. 97, 1545–1566.
Zeeb, C., Gomez-Rivas, E., Bons, P.D., Virgo, S., Blum, P., 2013b. Fracture network evaluation program (FraNEP): a software for analyzing 2D fracture trace-line maps. Comput. Geosci. 60, 11–22.